Asian Journal of Pharmaceutical Sciences 21 (2026) 101126

Available online at www.sciencedirect.com

ScienceDirect

journal homepage: www.elsevier.com/locate/AJPS



Research Article

In vivo self-assembled siRNAs targeting VEGFR2 and mTOR for renal cell carcinoma treatment

Jinyu Fu[a,b,#], *Xinyan Zhou*[b,#], *Junjie Mi*[b,#], *Likun Zhou*[d], *Luzhen Ma*[b], *Jingwei Guo*[b], *Jieqiong Lei*[b], *Shuang Qu*[b], *Zheng Fu*[b], *Tianyao Liu*[a], *Xi Chen*[a,b,c,*], *Rong Yang*[a,*]

[a] *Department of Urology, Nanjing Drum Tower Hospital, Affiliated Hospital of Medical School, Nanjing University, Nanjing 210993, China*
[b] *State Key Laboratory of Pharmaceutical Biotechnology, Jiangsu Engineering Research Center for MicroRNA Biology and Biotechnology, NJU Advanced Institute of Life Sciences (NAILS), School of Life Sciences, Nanjing University, Nanjing 210023, China*
[c] *The Second People's Hospital of Changzhou, The Third Affiliated Hospital of Nanjing Medical University, Changzhou Medical Center, Nanjing Medical University, Changzhou 213003, China*
[d] *Tianjin Medical University Cancer Institute and Hospital, National Clinical Research Center for Cancer, Tianjin's Clinical Research Center for Cancer, Key Laboratory of Cancer Prevention and Therapy, Tianjin Key Laboratory of Digestive Cancer, Tianjin 300171, China*

ARTICLE INFO

Article history:
Received 26 May 2025
Revised 3 November 2025
Accepted 24 December 2025
Available online 20 January 2026

Keywords:
Renal cell carcinoma
Small extracellular vesicle
Combination therapy
VEGFR2, MTOR

ABSTRACT

Renal cell carcinoma (RCC) is a challenging urologic malignancy characterized by its aggressive nature, including invasion, metastasis, and treatment resistance. To explore multi-targeted therapies, we established an advanced clear cell renal cell carcinoma (ccRCC) model via orthotopic tumor transplantation in mice, and established another model simulating post-surgical recurrence by performing radical nephrectomy. We engineered a genetic circuit to reprogram the host liver as a bioreactor, enabling the production and delivery of *in vivo* self-assembled siRNAs (IVSA-siRNAs) for co-targeting *VEGFR2* and *mTOR*. The efficacy and toxicity of this IVSA-siRNA system were evaluated and compared with the combination therapy of sunitinib and everolimus. In the established models, the combination therapy of sunitinib and everolimus showed efficacy but induced severe adverse effects. In contrast, IVSA-siRNAs potently silenced *VEGFR2* and *mTOR* expression, achieving therapeutic effects in both advanced and radical nephrectomy ccRCC models without discernible toxicity.

© 2026 Shenyang Pharmaceutical University. Published by Elsevier B.V.
This is an open access article under the CC BY-NC-ND license (http://creativecommons.org/licenses/by-nc-nd/4.0/)

1. Introduction

Renal cell carcinoma (RCC) is the third most prevalent urologic malignancy and carries the highest mortality rate among urologic cancers [1,2]. The predominant subtype, clear-cell renal cell carcinoma (ccRCC), accounts for 75%–85% of all RCC cases and is characterized by high rates of local invasion, metastasis, mortality, and resistance to conventional therapies [3]. According to the Tumor Node Metastasis (TNM)

* Corresponding authors.
E-mail addresses: xichen@nju.edu.cn (X. Chen), doctoryr@gmail.com (R. Yang).
# These authors contributed equally to this work.
Peer review under responsibility of Shenyang Pharmaceutical University.
https://doi.org/10.1016/j.ajps.2026.101126
1818-0876/© 2026 Shenyang Pharmaceutical University. Published by Elsevier B.V. This is an open access article under the CC BY-NC-ND license (http://creativecommons.org/licenses/by-nc-nd/4.0/)

staging system, RCC is classified as localized or advanced [4]. Radical nephrectomy is the standard initial treatment for localized RCC [5]. However, approximately 30% of RCC patients present with advanced disease, where surgery is not feasible, and require palliative care, including radiation therapy and chemotherapy [6]. Notably, a significant proportion of patients who undergo radical nephrectomy experience recurrence and metastasis postoperatively [7,8]. Therefore, it is crucial to implement perioperative systemic therapy, including neoadjuvant and adjuvant therapy. Neoadjuvant therapy aims to reduce tumor size before radical nephrectomy to improve surgical feasibility, while adjuvant therapy is administered postoperatively to eliminate micro-metastases [9,10]. Recent studies have shown that adjuvant therapy after radical nephrectomy for high-risk ccRCC can lower the likelihood of cancer recurrence and significantly reduce mortality risk by 48% [11]. Both neoadjuvant and adjuvant therapies encompass various modalities, including chemotherapy, endocrine therapy, and molecularly targeted therapy [12,13]. Despite these advancements, effective, safe, and consistent long-term management strategies for advanced RCC remain an unmet need, underscoring the necessity to develop novel approaches to prevent recurrence and metastasis.

Over the past few decades, the development of molecular targeted therapies against driver mutations and gene fusions has brought significant advancements in cancer treatment [14]. Many of these therapies are founded on the ''one molecule-one target-one disease'' paradigm [15]. Current drug development in molecular targeted therapy focuses on designing highly selective small-molecule inhibitors or monoclonal antibodies against individual targets [16–18]. This approach aims to modulate the biological function of a single molecular target, which is considered fully responsible for a specific disease, while minimizing the risk of adverse effects. However, cancer is a complex disease marked by the dysregulation of numerous genes and signaling pathways [3]. It is increasingly recognized that cancer cannot be effectively treated by monotherapy directed against a single pathway. To overcome this limitation, an alternative strategy focuses on simultaneously targeting multiple oncogenic proteins and pathways essential for tumor cell proliferation and survival [15,19]. Consequently, developing multi-target therapies has emerged as a major and promising frontier in cancer treatment [20]. Traditional multi-target therapies, also called combination therapy, typically entail using multiple targeted drugs concurrently, which commonly include distinct small-molecule inhibitors or combinations of inhibitors and antibody drugs. These therapies aim to target multiple pathways concurrently, thereby achieving additive or synergistic anti-cancer effects. Nevertheless, the therapeutic efficacy of combination therapies is often compromised by variations in pharmacokinetics, pharmacodynamics and bioavailability across the constituent drugs [21,22]. Additionally, these therapies face obstacles including high costs, complex dosing regimens, potential drug-drug interactions and cumulative toxicities [23,24]. For example, designing a combination therapy for advanced RCC presents a challenge of balancing effectiveness and safety. Sunitinib, an oral tyrosine kinase inhibitor (TKI) targeting the vascular endothelial growth factor receptor (VEGFR), is a first-line targeted drug for recurrent and unresectable RCC [3,25,26]. Everolimus, an oral inhibitor of the mechanistic target of rapamycin (mTOR), is approved for subsequent treatment after TKI therapy fails [3,26,27]. Given the critical roles of the VEGF and mTOR pathways in promoting RCC neovascularization and tumor growth, there is a strong rationale supporting combining sunitinib and everolimus to improve outcomes in advanced RCC [28,29]. However, this drug combination is linked to significant acute and chronic adverse effects, including mucositis, thrombocytopenia, anemia, fatigue, dehydration and hypoglycemia [30–32].

The ongoing evolution in multi-target therapy approaches is shifting from combining several single-targeted drugs toward using a single multi-targeted agent, which can provide superior therapeutic effects with fewer side effects [15,20,33,34]. Specifically, a single administration of a multi-targeted anti-cancer agent enables the simultaneous blockade of multiple oncoproteins and oncogenic pathways in cancer cells, leading to additive or synergistic therapeutic outcomes and a greater potential for eradicating cancer cells. Additionally, the development of a multi-targeted agent represents a more efficient and rational alternative to drug combinations. It simplifies the therapeutic regimen, avoids drug-drug interactions, eliminates differences in pharmacokinetics and pharmacodynamics, and reduces side effects arising from the cytotoxicity of individual drugs [35–37]. Overall, designing multi-targeted agents is more straightforward and potent than developing traditional combination therapies, offering an effective solution to overcome the major challenges of current anti-cancer drugs.

Molecular targeted therapies utilizing small interfering RNA (siRNA) for oncogene silencing have emerged as a promising therapeutic strategy for human cancers [38]. siRNAs bind to complementary mRNA sequences, leading to mRNA degradation and inhibition of protein synthesis [39]. Since siRNA action depends solely on mRNA sequence complementarity, they can specifically inhibit a wide range of genes, including those difficult to target with conventional therapies. Cellular delivery or expression of multiple siRNAs enables simultaneous targeting of different mRNAs, facilitating multi-gene silencing [40,41]. This approach offers opportunities to enhance therapeutic outcomes by sensitizing cancer cells to combination therapies. Moreover, designing a single expression cassette encoding multiple siRNAs allows their co-transcription, providing a simple and efficient strategy for the simultaneous multi-gene inhibitions. These multi-target siRNA therapeutics offer a powerful tool for dissecting complex gene networks, producing additive or synergistic anti-cancer effects, overcoming drug resistance, enhancing targeting, and reducing side effects in cancer therapy. However, the success of siRNA therapy is heavily dependent on delivery carriers that protect siRNA from degradation, facilitate cellular uptake, and promote endosomal escape into the cytoplasm for entry into the RNA interference (RNAi) pathway.

Currently, siRNA delivery vectors are primarily categorized into viral and non-viral types [42,43]. Among viral vectors,

adeno-associated virus (AAV) has become the predominant choice for *in vivo* delivery. By integrating siRNA into the viral genome, this approach utilizes the virus's natural infectivity to deliver siRNA into host cells [44]. However, viral vectors exhibit significant immunogenicity and cytotoxicity *in vivo*, and carry a risk of unintended gene integration, raising safety concerns [43]. Non-viral vectors are primarily based on lipid-based nanoparticles (LNPs) [45], which encapsulate siRNA for cellular entry via endocytosis and subsequent release. Nevertheless, non-viral vectors face challenges in delivery efficiency, cell specificity, immunogenicity and production costs [46]. Therefore, the development of an effective delivery system and administration route remains a major hurdle to fully realize the potential of siRNA-based therapies [47].

We have recently developed a synthetic biology strategy to reprogram the liver as a bioreactor for generating and delivering *in vivo* self-assembled siRNAs (IVSA-siRNAs) to specific tissues and cells [48]. This approach leverages the natural capability of the liver to express transgenes introduced via intravenous injection of genetic circuits in the form of naked DNA plasmids. Upon uptake by liver cells, the strategy utilizes the liver's endogenous small RNA processing machinery to generate siRNAs, which are subsequently packaged into secretory small extracellular vesicles (sEVs, <200 nm), naturally circulating sEVs then transport siRNAs to target tissues and cells. This strategy addresses the limitations of current techniques associated with assembling and delivering siRNAs, such as low efficiency, toxicity and complexity. Importantly, this strategy enables the simultaneous targeting of multiple key genes and pathways involved in cancer pathogenesis through a combinatory multi-targeted genetic circuit [40,48]. As a result, IVSA-siRNAs offer a potential solution to the bottleneck in multi-target therapy for RCC.

In this study, we developed a ccRCC model by injecting luciferase-labeled murine renal cancer cells (Luc-Renca) beneath the kidney capsule. After tumors progressed to an advanced stage (mimicking advanced ccRCC), we administered a multi-targeted genetic circuit co-targeting *VEGFR2* and *mTOR* in this model. The primary objective was to evaluate the synergistic therapeutic effect of IVSA-siRNAs in inhibiting tumor growth and metastasis, thereby prolonging survival of tumor-bearing mice and alleviating the adverse effects associated with tumor burden. In mice without overt distant metastases, we performed radical nephrectomy (simulating ccRCC after radical nephrectomy) followed by administration of the multi-targeted genetic circuit co-targeting *VEGFR2* and *mTOR*. This allowed us to evaluate the potential of IVSA-siRNAs to reduce post-nephrectomy mortality and recurrence risk.

2. Materials and methods

2.1. Materials

The murine renal cancer cell line Renca was purchased from Procell Life Science and Technology. Mouse hemangioendothelioma endothelial cells (EOMA) were obtained from FuHeng Biology. Human umbilical vein endothelial cells (HUVEC) were acquired from iCell Bioscience. VEGFR2 and CD31 were from Cell Signaling Technology. mTOR and cytokeratin C were from Abcam. Ki67 were from Servicebio. RIPA lysis buffer and protease inhibitors (PMSF, 1:100) were from Beyotime. RPMI-1640 medium, DMEM fetal bovine serum (FBS) were from Gibco. BCA assay and ECL reagents were from Thermo Scientific. α-Tubulin, CD63, CD9, TSG101 and albumin were from Proteintech. GAPDH was from Santa Cruz Biotechnology. Iodixanol was from Sigma-Aldrich. Six-week-old male BALB/c mice were obtained from the Model Animal Research Center of Nanjing University. The animals were maintained under specific pathogen-free (SPF) conditions in a temperature-controlled room with a 12-h light/dark cycle and had free access to water and standard laboratory chow. All animal experiments were conducted in accordance with the Guide for the Care and Use of Laboratory Animals (National Institutes of Health Publication 85-23, revised in 1996) and were approved by the Animal Ethics and Welfare Committee of Nanjing University (approval number: IACUC-2205004). Mice were euthanized by carbon dioxide inhalation.

2.2. Design and construction of the genetic circuits

The siR-V and siR-mT circuits were generated by inserting a VEGFR2 siRNA or mTOR siRNA sequence (Table S1) into a 166-base pair miR-155 precursor framework. This framework retains the necessary nucleotide modifications to ensure proper base pairing (Table S2). To achieve co-expression of VEGFR2 siRNA and mTOR siRNA, the siR-V+mT circuit was constructed using pre-miR-155 backbone incorporating both siRNA sequences, with the mTOR siRNA sequence inserted downstream of the VEGFR2 siRNA sequence. A circuit expressing scrambled RNA (scrR) was used as a negative control. The genetic circuits were synthesized and assembled by Realgene Biotech. After transformation into *Escherichia coli* DH5α (Tsingke), the cells were cultured in LB medium supplemented with 50 μg/ml spectinomycin at 37 °C with shaking for 14 h. Subsequently, the plasmids were then extracted and purified using the Endo Free Maxi Plasmid Kit V2 (Tiangen). Sequencing confirmation was performed to confirm the authenticity of the acquired genetic circuit sequences.

2.3. Cell culture and transfection

Renca and HUVEC cells were cultured in RPMI-1640 medium. EOMA cells were cultured in DMEM. All media were supplemented with 10% FBS, 100 u/ml penicillin and 100 u/ml streptomycin in a humidified atmosphere of 5% CO_2 at 37 °C. All cell lines were authenticated by short tandem repeat (STR) profiling. Upon arrival, cells were expanded and subsequently cryopreserved in liquid nitrogen. For experimental purposes, cryopreserved vials were thawed and utilized within a two-month timeframe. Regular mycoplasma testing confirmed the absence of mycoplasma contamination in all cell lines. Transfection was performed using Lipofectamine 2000 reagents (Invitrogen) following the manufacturer's instructions.

2.4. Generation of luciferase-transduced cells

Stable Luc-Renca cells expressing firefly luciferase were established using lentiviral vectors encoding puromycin resistance. The luciferase lentiviral vector was obtained from Corues Biotechnology, and cells were transduced according to the manufacturer's instructions at an MOI of 10 in the presence of 5 μg/ml polybrene. Transduced cells were then selected with 5 μg/ml puromycin (Invitrogen). *In vitro* bioluminescence activity of Luc-Renca cells was evaluated using the IVIS™ bioimaging system with VivoGlo™ Luciferin (Promega) as the substrate.

2.5. Experimental protocol of the murine RCC model

2.5.1. Orthotopic ccRCC model

Six-week-old male BALB/c mice underwent the subrenal capsule implantation. A 10% solution of sodium pentobarbital (60 μl/20 g) was administered intraperitoneally to induce general anesthesia during surgery, and body temperature was maintained using a heating block. The left flank was shaved and disinfected with 75% ethanol, and the mouse was positioned laterally. A 1–2 cm incision was made along the midline of the left costal margin, and the left kidney was exposed by blunt dissection. The subrenal capsule of the left kidney was implanted with 1×10^5 Luc-Renca cells in 25 μl of phosphate-buffered saline (PBS) /Matrigel (2:1, v/v). The incision was then closed with sutures, and the mice were allowed to recover. Tumor engraftment was monitored by *in vivo* bioluminescence imaging (BLI) using the IVIS™ bioimaging system after intraperitoneal injection of VivoGlo™ Luciferin (Promega) following the manufacturer's protocol.

2.5.2. Radical nephrectomy of ccRCC mice

For nephrectomy, the surgical site was disinfected, and mice were anesthetized. A flank incision was made to expose the tumor-bearing left kidney. The renal artery, vein and ureter were ligated using 4–0 surgical sutures, and the kidney was excised. Hemostasis was confirmed before wound closure with interrupted sutures. Body temperature was maintained throughout the procedure. Mice were returned to their cages after recovery from anesthesia for postoperative monitoring.

2.5.3. Drug administration

The scrR, siR-V, siR-mT and siR-V+mT circuits (10 mg/kg) were delivered intravenously via the tail vein, while 100 μl PBS was delivered as a control. For small molecule inhibitor therapy, the groups received 20 mg/kg of sunitinib (Suni), everolimus (Evm), sunitinib plus everolimus (Combo), or 100 μl vehicle (0.1% dimethyl sulfoxide (DMSO), v/v) (PBO) via oral gavage.

2.6. Histological staining

Hematoxylin and Eosin (H&E) staining was performed according to standard laboratory protocols. Tissues samples from the heart, liver, lung and tumor were dehydrated through a graded ethanol series, cleared in xylene, and embedded in paraffin. Paraffin sections were cut, air-dried and then deparaffinized in xylene, rehydrated through graded ethanol series, and stained sequentially with H&E. After quick dehydration, the slides were mounted with a coverslip. Tumor burden and inflammatory infiltration were assessed blindly by pathologists. Cardiomyocyte diameter was quantified using Image Pro Plus software for statistical analysis.

2.7. Echocardiography

Mice were anesthetized with isoflurane via an inhalation system and positioned on a heating platform maintained at 37 °C. Cardiac function was assessed using echocardiography at the Experimental Animal Center of Nanjing Medical University. Measured parameters included left ventricular ejection fraction (EF), heart mass, fractional shortening (FS), left ventricular mass (LV Mass), left ventricular volume in end-diastole (LV VOLd), left ventricular volume in end-systole (LV VOLs), interventricular septal thickness in end-systole (IVSs), interventricular septal thickness in end-diastole (IVSd), left ventricular internal diameter in end-diastole (LVIDd), left ventricular internal diameter in end-systole (LVIDs), left ventricular posterior wall thickness in diastole (LVPWd), and left ventricular posterior wall thickness in systole (LVPWs).

2.8. Analyses of serum biochemical indicators

Serum biochemistry was analyzed to evaluate hepatocellular integrity. Levels of alanine aminotransferase (ALT), aspartate aminotransferase (AST) and alkaline phosphatase (ALP) were measured by Wuhan Servicebio Biotechnology. Additionally, the concentrations of total cholesterol, triglycerides and free fatty acids in the serum were determined using corresponding commercial assay kits (Nanjing Jiancheng Bioengineering Institute) to assess lipid metabolism profiles.

2.9. Immunohistochemistry

Immunohistochemistry (IHC) was performed according to established protocols. Tumor and lung tissue samples were fixed in paraformaldehyde, dehydrated through a graded ethanol series, cleared in xylene, and embedded in paraffin. Paraffin-embedded sections were cut and air-dried overnight. The sections were then deparaffinized in xylene, rehydrated through a graded ethanol series, and subjected to antigen retrieval by heating in citrate buffer for 8 min. Endogenous peroxidase activity was quenched by exposing the sections to 3% hydrogen peroxide for 30 min. The sections were then incubated overnight at 4 °C with primary antibodies specific to VEGFR2, CD31, mTOR, Ki67 and cytokeratin C, all diluted in appropriate buffer systems. After washing, the sections were incubated with species-specific secondary antibodies for 1 h at room temperature, followed by incubation with avidin-biotin complex (ABC) reagent for 30 min. Immunoreactivity was visualized using DAB (Boster Biological Technology) for 5 min. Nuclei were counterstained with hematoxylin (YEASEN), and the sections were dehydrated through a graded ethanol series. The stained slides were independently assessed by experienced pathologists blinded to the experimental conditions. Quantitative analysis was

performed using ImageJ software (NIH) to evaluate the staining intensity and distribution.

2.10. Protein isolation and western blot (WB) analysis

Total protein was extracted from tissue and cell samples using RIPA lysis buffer supplemented with protease inhibitors (PMSF, 1:100). After incubation on ice for 40 min, the supernatant was collected by centrifugation at 12,000 g for 10 min at 4 °C. Protein concentrations were determined using the BCA assay according to the manufacturer's instructions. Thirty micrograms of total protein per lane were separated by SDS-PAGE and transferred to PVDF membranes. The membranes were blocked with 5% skimmed milk in TBST for 1 h at room temperature and then incubated with the primary antibodies for 2 h at room temperature. The antibodies used were as follows: VEGFR2; mTOR; α-Tubulin; GAPDH. For the detection of sEV markers, the following antibodies were used: CD63, CD9, TSG101 and Albumin. Primary antibodies were incubated overnight at 4 °C, followed by secondary antibodies (HRP-conjugated) for 1 h at 37 °C. The blots were visualized using ECL reagents and band intensities were quantified using ImageJ software (National Institutes of Health). Protein levels were normalized to those of α-Tubulin, which served as the loading control.

2.11. Evaluation of genetic circuit accumulation in vivo

Plasmid DNA was extracted from liver, lung, and kidney tissues (~100 mg each) using a plasmid extraction reagent kit (TIANGEN Biotech). To quantify the siR-V circuit, in the form of a DNA plasmid, a standard curve was generated by qPCR using serially diluted siR-V circuit and plotting the cycle threshold (Ct) values against the log of the input amount. The Ct values of the siR-V circuit in tissue DNA samples were then measured, and the plasmid copy numbers were determined using the standard curve.

2.12. RNA isolation and quantitative RT-PCR assay

Total RNA was extracted from tissues and cells using TRIzol reagent (Sigma). For mRNA quantification, 1 μg of total RNA was reverse-transcribed into cDNA using HiScript III RT SuperMix for qPCR (+gDNA wiper) (Vazyme). Subsequently, qPCR was performed using gene-specific primers and ChamQ SYBR qPCR Master Mix (Vazyme) to amplify mTOR, VEGFR2 and GAPDH transcripts, with GAPDH serving as an internal control. The reactions were performed in a 96-well optical plate, with an initial incubation at 95 °C for 5 min, followed by 40 cycles of 95 °C for 10 s and 60 °C for 30 s. Data analysis was conducted using the $2^{-\Delta\Delta Ct}$ method, calculated using the formula: $\Delta\Delta Ct=(\Delta Ct_{target}) - (\Delta Ct_{control})$ and $\Delta Ct = Ct_{target\ gene} - Ct_{GAPDH}$.

For absolute quantification of siRNA, 100 ng of total RNA was reverse-transcribed into cDNA using AMV reverse transcriptase (TaKaRa). The qPCR reactions were performed in a 96-well optical plate with an initial denaturation at 95 °C for 10 min, followed by 40 cycles of 95 °C for 30 s, 60 °C for 30 s, and 72 °C for 30 s. A standard curve was generated from serial dilutions of synthesized siRNA. The siRNA concentration in different tissues was quantified by interpolation from the standard curve, and expressed as the absolute amount per gram of total RNA (pmol/g RNA).

Each reaction was performed in triplicate, and the CT values were determined using consistent fluorescence threshold settings. The primer sequences are listed in Tables S3 and S4.

2.13. sEV isolation and characterization

2.13.1. sEV isolation

Approximately 1 ml venous blood was collected from mice into plasma separator tubes. Plasma was separated by centrifugation at 800 g for 10 min at room temperature. Crude extracellular vesicles (EVs) were then isolated through sequential differential centrifugation: 500 g for 5 min, 3000 g for 25 min, 10,000 g for 1 h, and 120,000 g for 1.5 h, all at 4 °C. For high-purity vesicle isolation, density gradient centrifugation was performed. An iodixanol density gradient (18%, 24%, 30% and 36% in PBS) was prepared. The crude EV pellet was resuspended in iodixanol to a final concentration of 36% [49]. The gradient was carefully layered by overlaying with descending iodixanol concentrations. After centrifugation at 120,000 g for 14 h at 4 °C, the 6 ml fraction from the top of the gradient was collected, diluted 12-fold with particle-free PBS, and subjected to ultracentrifugation at 120,000 g for 4 h at 4 °C. The resulting fractions were diluted in particle-free PBS for nanoparticle tracking analysis (NTA) and transmission electron microscopy (TEM) analysis [50], and the other part was lysed for subsequent RNA or protein extraction.

2.13.2. NTA

The isolated sEVs were diluted in particle-free PBS, passed through a 0.22-μm filter, and analyzed using a Nanosight NS300 system equipped with a 488-nm blue laser. All samples were analyzed in parallel, and a minimum of three video recordings were captured and analyzed using NTA software to determine particle concentration and size distribution. The average value across all video recordings was used to generate a representative size distribution profile.

2.13.3. Electron microscopy

The isolated sEVs were suspended in PBS and applied onto a carbon-coated copper grid. After a 2-min incubation, the excess liquid was carefully blotted away with filter paper. The samples were then negatively stained with a 3% phosphotungstic acid for 5 min, air-dried, and imaged using a KYKY-EM3200 TEM.

2.14. EdU assay

Cell proliferation was evaluated using an EdU Cell Proliferation Kit (Ribobio) according to the manufacturer's instructions. Renca or EOMA cells were seeded at a density of 2×10^4 cells per well in 48-well plates. The cells were cultured in a humidified incubator at 37 °C with 5% CO_2 for 12 h, followed by fixation with 4% paraformaldehyde and staining using the EdU Cell Proliferation Kit. Images were acquired using a laser scanning confocal microscope (Carl

Zeiss LSM 800) and analyzed with ImageJ software to quantify the percentage of EdU-positive cells.

2.15. Angiogenesis assay

For the angiogenesis assay, a 96-well plate was coated with Matrigel matrix (Corning) and incubated at 37 °C for 30 min to allow polymerization. Stably transfected HUVEC cells were then seeded onto the matrigel-coated wells at a density of 5×10^3 cells per well. After incubation at 37 °C in a 5% CO_2 humidified atmosphere for 6 h, morphological changes were visualized using a microscope. Each experiment was performed in triplicate, and the number of nodes was quantified using ImageJ software.

2.16. Assessment of apoptosis

After transfection with siR-mT or siR-V+mT circuits, the cell culture medium was replaced with serum-free RPMI 1640 medium and incubated for 24 h. The cells were then dissociated into a single-cell suspension, washed with PBS, and resuspended in cold binding buffer at a concentration of 1×10^6 cells/ml. Apoptosis in Renca cells was detected using the FITC-Annexin V Apoptosis Detection Kit I (BD Bioscience). The cell suspension was incubated with FITC-Annexin V and propidium iodide (PI) at room temperature in the dark for 15 min, and apoptotic cells were quantified by flow cytometry. For detection of apoptosis in primary liver cells, the TUNEL assay (Promega) was performed. Primary liver cells were extracted, fixed with 4% paraformaldehyde, permeabilized in 70% cold ethanol, and stored at −20 °C. The following day, the cells were stained according to the manufacturer's protocol and analyzed using flow cytometry to assess apoptosis. Fluorescence intensity was analyzed to determine the apoptosis rate.

2.17. Statistics and reproducibility

Quantitative analysis of immunohistochemical and histological results was performed using Image-Pro Plus software (Media Cybernetics). Flow cytometry data were analyzed with FlowJo V10 (BD Biosciences). qPCR results were analyzed with Microsoft Excel (Microsoft Corporation). WB results with ImageJ (National Institutes of Health). BLI results with Living Image® software (PerkinElmer). Detailed statistical information is provided in the figure legends. All statistical tests were performed using GraphPad Prism 9 (GraphPad Software). Survival rates were represented using Kaplan-Meier curves. The normality of the data was tested using the Shapiro-Wilk test. Comparisons between two groups were performed using the two-tailed unpaired Student's *t*-test. Differences between three or more groups were compared by one-way ANOVA followed by Dunnett's test for multiple comparisons. For experiments involving two independent factors, two-way ANOVA followed by Dunnett's test was employed. The sample size (n) for each experimental group is specified in the figure legends. Values are presented as the mean ± standard error of the mean (SEM). Statistical significance is denoted as $^{*}P < 0.05$, $^{**}P < 0.01$, $^{***}P < 0.001$, $^{****}P < 0.0001$.

3. Results and discussion

3.1. Construction of mouse model of ccRCC

To address the challenges of treating advanced RCC, we established two animal models that recapitulate the tumor microenvironment and spontaneous metastasis of ccRCC. For the advanced ccRCC model, luciferase-expressing Renca cells (Luc-Renca) were injected under the renal capsule of BALB/c mice (Fig. S1A). BLI confirmed disease progression to metastatic ccRCC, with lung metastases detectable from Day 13 (Fig. S1B–S1C) [51]. Histological examination of orthotopic tumor and lung tissue supported these findings (Fig. S1D–S1E). The advanced ccRCC model was used to evaluate the therapeutic potential of IVSA-siRNAs in suppressing tumor progression and metastasis, as well as alleviating tumor burden.

To simulate ccRCC after radical nephrectomy, mice with orthotopic tumors underwent radical nephrectomy at the appropriate stage (Fig. S2A). Successful engraftment and tumor growth were confirmed by BLI at 3-d and 10-d post-implantation (Fig. S2B–S2D). On Day 10, all mice underwent radical nephrectomy before detection of lung metastasis, mimicking surgery in the absence of metastasis. By Day 28, substantial lung metastases were observed (Fig. S2B, S2C and S2E), reflecting post-surgical recurrence. This radical nephrectomy ccRCC model was utilized to evaluate the therapeutic efficacy of the IVSA-siRNAs in reducing mortality and recurrence risk after radical nephrectomy.

3.2. Assessment of efficacy and toxicity in combined therapy for advanced ccRCC

The efficacy of the combination therapy with sunitinib and everolimus was evaluated in the mouse model of advanced ccRCC. BLI on Day 3 confirmed successful tumor engraftment and a consistent initial tumor burden across all mice (Fig. S3A). On Day 13, mice were randomly assigned to four treatment groups: placebo (PBO, as a control), combination therapy of sunitinib and everolimus (Combo), sunitinib alone (Suni) and everolimus alone (Evm) (Fig. 1A). Survival analysis showed that the median survival time was significantly extended from 23 d in the PBO group to 61 d in the Combo group, demonstrating a significant improved survival in both the Combo groups. (Fig. 1B). Furthermore, BLI at Day 28 revealed that the size of orthotopic tumors in the Combo and Evm groups was reduced by 74% compared with those in the PBO group (Fig. 1C–D). Concurrently, BLI at Day 28 revealed that the lung fluorescence intensity in the Combo group was reduced by 45% compared to that in the PBO group, indicating a significantly lower extent of lung metastases (Fig. 1E–F). Histological evaluation confirmed a substantial reduction in lung metastases in the Combo and Suni groups (Fig. 1G). These results suggest distinct therapeutic advantages of sunitinib and everolimus individually: everolimus was more effective against orthotopic renal tumors, while sunitinib excelled in controlling lung metastases. The combination therapy achieved the optimal control of both orthotopic tumor growth

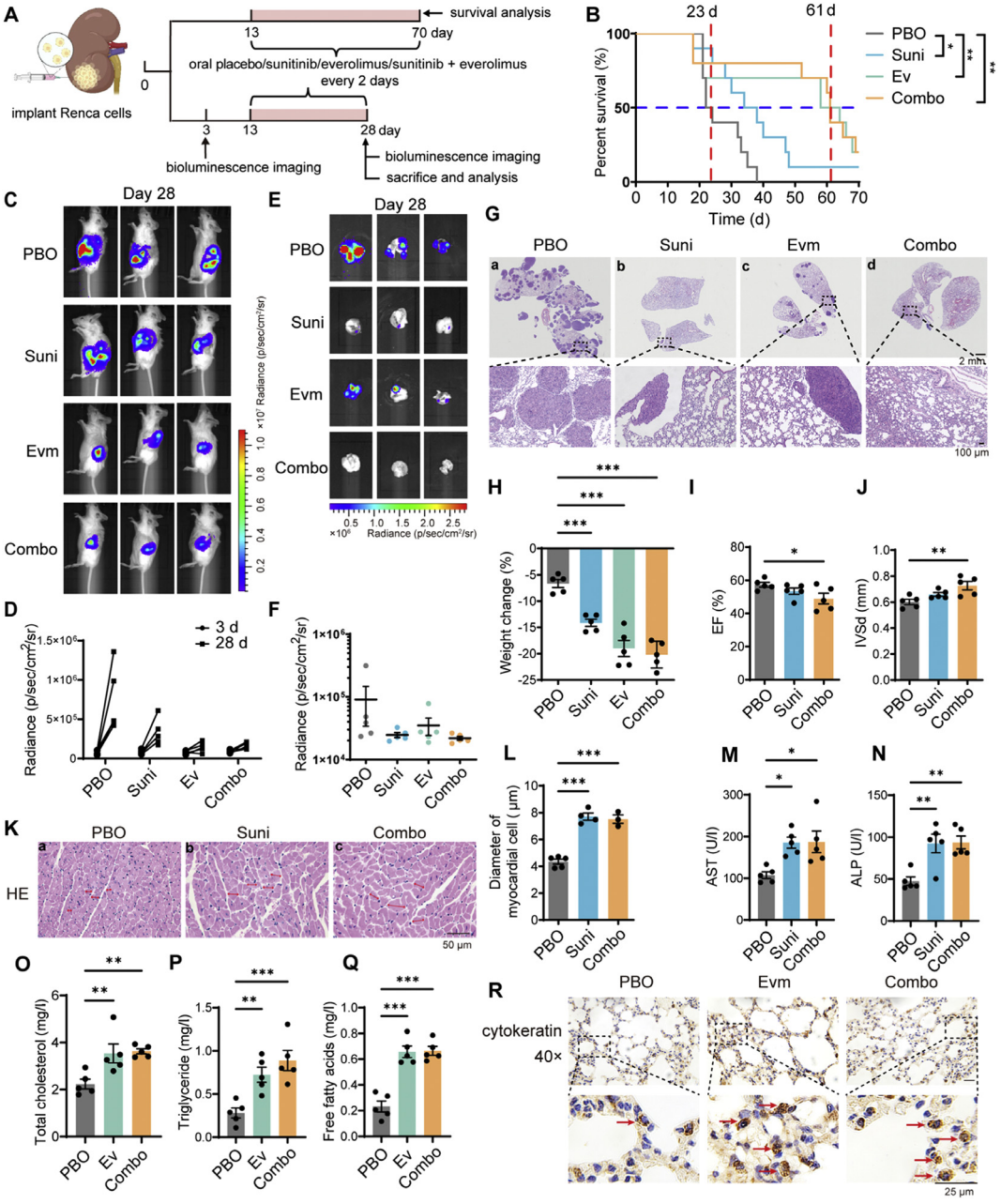


Fig. 1 – Assessing the efficacy and toxicity of combination therapy for advanced ccRCC mice. (A) Schematic illustration of the experimental design; (B) Kaplan-Meier survival curves ($n = 10$), the dashed lines at 23 d and 61 d indicate the median survival duration for the PBO group and Combo group, respectively; (C) Luminescent images of mice and (E)lung metastases on Day 28; (D) Quantitative BLI results for each mouse ($n = 5$) and (F) lung metastases ($n = 5$); (G) H&E-stained lung sections. (a-c) H&E staining at 40 × and 100 × magnifications demonstrate epithelial-like structures with cellular atypia and focal nests or cord-like arrangements. These features are consistent with a metastatic carcinoma. (d) Demonstrate normal lung tissue. Scale bar: 2 mm (upper panel) and 100 μm (lower panel); (H) Ratio of body weight change ($n = 5$); (I) Left ventricular EF of treated mice ($n = 5$); (J) Interventricular septal thickness in end-diastole (IVSd) ($n = 5$); (K) (a) H&E staining at 100 × magnification demonstrates normal myocardial tissue. (b,c) Demonstrate significantly enlarged cardiomyocyte volumes with abundant cytoplasm, the nuclei are enlarged and pleomorphic. These features are consistent with myocardial hypertrophy. The red double arrows indicate the cross-sectional area of cardiomyocytes, highlighting the morphological changes. Scale bar: 50 μm; (L) Average diameter of myocardial cells ($n = 3$–5); Serum (M) AST and (N) ALP enzyme activity ($n = 5$); (O) Total cholesterol, (P) triglyceride and (Q) free fatty acid levels in serum ($n = 5$); (R) Images of lung sections stained with cytokeratin. Arrows indicate hyperplastic enlarged foamy pneumocytes. Scale bar: 25 μm. Values are presented as the mean ± SEM. Significance was determined using one-way ANOVA followed by Dunnett's multiple comparison or Kaplan-Meier test for survival analysis. *$P < 0.05$; **$P < 0.01$; ***$P < 0.001$.

and lung metastasis, demonstrating its enhanced therapeutic efficacy.

However, sunitinib has been reported to exhibit cardiotoxicity and hepatotoxicity [52–54], while everolimus has been associated with lung injury and disrupted lipid metabolism [55]. Therefore, a comprehensive safety assessment of the combination therapy is essential for the Combo group. On Day 28, the Combo group exhibited the greatest reduction in body weight compared to the other groups (Fig. 1H). Furthermore, echocardiography assessment revealed impaired cardiac performance in the Combo group, characterized by a significant increase in heart mass (Fig. S3B), a decreased left ventricular EF (Fig. 1I), and a notable increase in IVSd (Fig. 1J), while other cardiac indices remained unchanged (Fig. S3C-S3K). Histological evaluation of transverse heart sections showed significant myocardial hypertrophy in the Combo group, with a substantial increase in muscle fiber diameter, approximately twice that of the control PBO group (Fig. 1K–1L). Additionally, the Combo group showed a slight increase in liver weights (Fig. S3L), along with significantly elevated serum levels of ALT (Fig. S3M), AST (Fig. 1M) and ALP (Fig. 1N). Moreover, the TUNEL assay revealed increased apoptotic cells in the liver of the Combo group (Fig. S3N–S3O). Histological staining of liver sections from the Combo and Suni groups indicated immune cell infiltration (Fig. S3P). Serum levels of cholesterol, triglycerides and free fatty acids were significantly elevated in the Combo and Evm groups compared to the PBO group (Fig. 1O–1Q). Histopathological examination of lung sections showed notable foamy changes in enlarged pneumocytes, as demonstrated by cytokeratin staining, in the Combo and Evm groups (Fig. 1R) accompanied by immune cell infiltration (Fig. S3Q). Together, these results indicated that prolonged combination therapy with sunitinib and everolimus resulted in impaired cardiac function, systemic lipid metabolism disturbances, and alveolar epithelial damage.

3.3. *Characterization of the IVSA-siRNA targeting solely VEGFR2*

To target *VEGFR2* with IVSA-siRNA, we engineered a genetic circuit comprising two functional modules: a promoter for siRNA transcription and sEVs packaging, and an siRNA expression cassette module designed to maximize guide strand expression while minimizing passenger strand generation. Building on our previous work [48], we selected the cytomegalovirus (CMV) promoter as the optimal promoter module and the pre-miR-155 backbone as the siRNA expression cassette. By inserting the VEGFR2 or mTOR siRNA sequence into the 5′ arm of the pre-miR-155 hairpin structure, we constructed three CMV-driven genetic circuits (as DNA plasmids) for expressing VEGFR2 siRNA (siR-V) or mTOR siRNA (siR-mT), respectively (Fig. S4A- S4B and Table S1 and S2). The siR-V and siR-mT circuits were constructed and validated individually.

We then evaluated the functionality of the three siR-V circuits *in vitro* to confirm their ability to produce functional VEGFR2 siRNA (Fig. S5A). To rule out false-positive results from differential plasmid uptake, we first confirmed equivalent transfection efficiencies across the three siR-V circuits (each containing a GFP gene) in EOMA cells by fluorescence imaging and flow cytometry (Fig. S5B-S5E). EOMA cells were then transfected with the three siR-V circuits targeting distinct coding sequence (CDS) regions of *VEGFR2*, and *VEGFR2* expression was analyzed by quantitative RT-PCR and WB, using a CMV-driven genetic circuit encoding scrR as the negative control. Transfection with the third siR-V circuit reduced *VEGFR2* expression at both mRNA and protein levels (Fig. S5F-S5H). Based on these results, the third siR-V circuit was selected for all subsequent experiments.

Angiogenesis, the formation of new blood vessels from pre-existing ones, is critical for normal tissue development and tumor progression and metastasis [56]. *VEGF* binding to *VEGFR2* activates downstream signaling that promotes endothelial cell proliferation, survival, migration, and vascular permeability [57]. To assess the effects of the selected siR-V circuit, we conducted EdU proliferation assays and angiogenesis assays using transfected EOMA cells and HUVEC cells, respectively. The results show that the siR-V circuit significantly inhibited EOMA cell proliferation (Fig. S5I-S5J) and suppressed angiogenesis in HUVEC cells (Fig. S5K–S5L).

The siR-V circuit was constructed as a naked DNA plasmid and administered intravenously to mice via the tail vein. Given that the liver naturally takes up naked DNA plasmids and expresses transgenes [48,58], the siR-V circuit is preferentially taken up by the mouse liver, where it is processed by the endogenous miRNA machinery to generate miRNA-like VEGFR2 siRNA in hepatocytes. Subsequently, cytoplasmic VEGFR2 siRNA is spontaneously packaged into secretory sEVs and released into the bloodstream from the liver. To validate hepatic-specific plasmid retention and expression, BALB/c mice were injected with scrR or siR-V circuits (10 mg/kg). The siR-V circuit rapidly accumulated in the liver within 1 h and returned to baseline levels by 6 h, but no significant accumulation of the siR-V circuit was detected in other tissues (Fig. S5M). Plasmid integrity and uptake in the liver at 1 h were confirmed by PCR and transformation of extracted liver DNA (Fig. S5N-S5P). Furthermore, GFP expression in liver sections collected 12 h after the injection of the GFP-gene-contained siR-V circuit confirmed functional plasmid expression *in vivo* (Fig. S5Q-S5R). To identify the recipient hepatic cell type, primary cells were isolated 19 h post-injection. Hepatocytes, Kupffer cells and liver sinusoidal endothelial cells (LSECs) were separated (Fig. S5S-S5T) and cultured. RT-qPCR analysis of both cells and their secreted sEVs revealed that VEGFR2 siRNA was predominantly detected in hepatocytes and hepatocyte-derived sEVs (Fig. S5U-S5V). In summary, the intravenously delivered siR-V circuit is preferentially taken up by hepatocytes, leading to the secretion of sEVs loaded with VEGFR2 siRNA.

Owing to the unique architecture of the siR-V circuit, previous studies have demonstrated that the siRNA generated by the circuit may associate with the sEV-rich fraction in the plasma [59–62]. Consequently, we investigated the distribution of VEGFR2 siRNA in the plasma (Fig. 2A). In siR-V-injected mice, a time-dependent pattern of VEGFR2 siRNA accumulation and clearance was observed in the plasma, peaking at 6 h post-injection and returning to baseline by 48 h (Fig. 2B). Previous studies have proposed two mechanisms for the stability of circulating miRNAs against ubiquitous

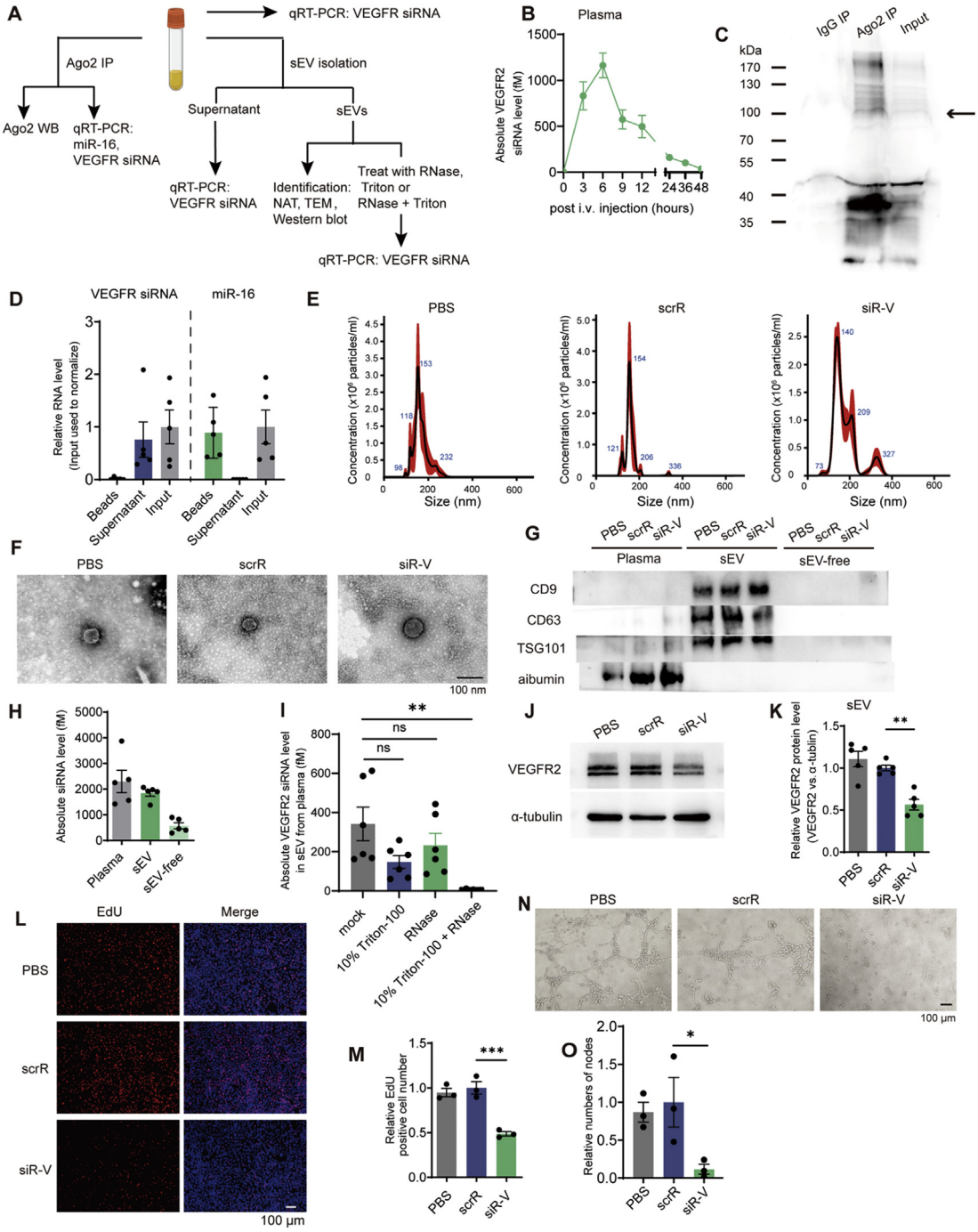


Fig. 2 – Evaluation of the self-assembly of VEGFR2 siRNA-encapsulating sEVs. (A) Schematic of the experimental design. (B) Kinetics of VEGFR2 siRNA in plasma ($n = 4$). (C) WB confirmed the specificity of Ago2 enrichment. (D) Quantitative RT-PCR to evaluate the recovery rates of miR-16 and VEGFR2 siRNA ($n = 5$). (E) Size distribution and concentration of purified sEVs determined by NTA ($n = 3$). (F) TEM images of sEVs. Scale bar: 100 nm; (G) WB of specific sEV markers. An equal amount of total protein was loaded in each lane; (H) Quantitative RT-PCR analysis of VEGFR2 siRNA in sEVs ($n = 5$); (I) Quantitative RT-PCR was used to assess the stability of VEGFR2 siRNA in sEVs ($n = 6$); (J) WB of VEGFR2 protein expression; (K) Quantification of relative VEGFR2 protein level ($n = 5$); (L) EdU staining of EOMA cells. Scale bar: 100 μm; (M) Quantification of the relative proportion of EdU-positive cells ($n = 3$); (N) Angiogenesis assay. Scale bar: 100 μm; (O) Quantification of the number of nodes ($n = 3$). Values are presented as the mean ± SEM. Significance was determined using one-way ANOVA followed by Dunnett's multiple comparison. *$P < 0.05$; **$P < 0.01$; ***$P < 0.001$.

blood RNases: (1) stabilization through association with RNA-binding proteins such as Argonaute-2 (Ago2), and (2) protection by EV membranes. To determine whether Ago2 protects VEGFR2 siRNA from plasma RNases, we analyzed VEGFR2 siRNA levels in Ago2-immunoprecipitated (IP) beads. Plasma from mice injected with the siR-V circuit was immunoprecipitated using control IgG or anti-Ago2 antibodies, and the precipitates were analyzed for miR-16 and VEGFR2 siRNA to assess their association with Ago2. WB confirmed Ago2-specific precipitation, as shown by a ~97 kDa band present only in Ago2 immunoprecipitates (Fig. 2C). Quantitative RT-PCR revealed that miR-16 was largely depleted from the plasma by Ago2 immunoprecipitation and enriched in the beads, whereas VEGFR2 siRNA was not captured by the anti-Ago2 antibody (Fig. 2D). These findings partially ruled out the mechanism of siRNA stability in circulation based on Ago2 protection. Subsequently, we analyzed the sEVs isolated from the plasma of mice injected with the scrR or siR-V circuit. First, we characterized the physical properties of the isolated sEVs [49,50]. NTA revealed that sEVs purified from scrR- or siR-V circuit-injected mice exhibited a typical nanoparticle size distribution, with a peak at approximately 150 nm (Fig. 2E). The concentration of sEVs in the plasma of siR-V circuit-injected mice was comparable to those from PBS-injected mice (Fig. 2E). TEM analysis confirmed that the purified sEVs displayed a distinctive spherical vesicular structure (Fig. 2F). CD63, CD9 and TSG101 are established protein markers for identifying sEVs, and their detection validates the successful isolation of authentic sEVs (Fig. 2G). Furthermore, a significant amount of VEGFR2 siRNA was detected within plasma sEVs from siR-V circuit-injected mice, whereas no VEGFR2 siRNA was detected in sEV-free plasma (Fig. 2H). To confirm that the siRNA was encapsulated within sEVs and protected by their lipid bilayer, we assessed their sensitivity to RNase in the presence and absence of Triton X-100-mediated membrane disruption. Plasma sEVs were divided into four groups: untreated, Triton X-100-treated, RNase-treated and treated with both RNase and Triton X-100. VEGFR2 siRNA levels remained stable in RNase-treated sEVs but were eliminated when both RNase and Triton X-100 were applied (Fig. 2I). This result confirms that the siRNA was encapsulated within the sEVs, rather than being a contaminant from the purification process. Finally, we validated the biological function of the sEVs generated in circulation following siR-V circuit injection. The addition of plasma sEVs to the culture medium of EOMA and HUVEC cells resulted in reduced *VEGFR2* expression at both mRNA and protein levels in EOMA cells (Fig. 2J–2K), as well as inhibited EOMA cell proliferation (Fig. 2L–2M) and HUVEC angiogenesis (Fig. 2N–2O). These findings demonstrate that VEGFR2 siRNA-encapsulating sEVs are present in the mouse circulatory system following siR-V circuit injection.

Previous studies have demonstrated that inhibiting VEGFR2 can impede tumor neovascularization, a key mechanism underlying the anticancer effects of sunitinib [56,57]. Therefore, we evaluated the therapeutic effects of IVSA-siRNA targeting *VEGFR2* in an orthotopic ccRCC model (Fig. S6A). On Day 3, BLI confirmed successful tumor engraftment and consistent initial tumor burden across all mice (Fig. S6B). Subsequently, the mice were treated every other day starting from Day 3 with PBS, scrR, siR-V or sunitinib. On Day 10, all mice underwent radical nephrectomy, and tumor tissues were collected. BLI was performed on Day 28 to assess lung metastases. IHC for CD31, a marker of vascular endothelial cells [63], was used to evaluate microvascular density. In the siR-V group, we observed substantial accumulation of VEGFR2 siRNA in the liver, kidney, orthotopic tumor and lung metastatic (Fig. S6C-S6E), which corresponded with reduced VEGFR2 mRNA levels in both orthotopic and lung metastatic tumors (Fig. S6F-S6G). Compared to mice treated with PBS or scrR, those treated with siR-V or sunitinib exhibited significant but modest inhibition of orthotopic tumor growth (Fig. 3A–3B and S6H). Notably, the siR-V circuit effectively downregulated VEGFR2 protein expression in orthotopic tumor (Fig. 3C–3D and S6I-S6J), leading to a comparable anti-angiogenic effect (Fig. S6I and S6K). Furthermore, the siR-V circuit significantly impeded the formation and proliferation of lung metastases (Fig. 3E–3G) by reducing microvessel density within the metastatic (Fig. 3H–3I). Consistently, the siR-V circuits also suppressed *VEGFR2* expression in lung metastatic (Fig. S6L-S6O). Overall, the siR-V circuit enabled efficient production of VEGFR2 siRNA and its encapsulation into plasma sEVs, leading to the *VEGFR2* suppression in endothelial cells via IVSA-siRNA mechanism. Thus, the IVSA-siRNA targeting *VEGFR2* exhibited significant effectiveness in inhibiting neovascularization and lung metastasis.

3.4. *Characterization of the IVSA-siRNA targeting solely mTOR*

Similarly, we designed three *mTOR*-targeting circuits (siR-mT) (Fig. S4B and Table S1 and S2) and evaluated their efficacy *in vitro* (Fig. S7A). Prior to the screening of siR-mT circuits, we transfected EOMA cells with the three siR-mT circuits containing a GFP gene and demonstrated equivalent transfection efficiencies by fluorescence imaging and flow cytometry (Fig. S7B–S7E), thereby ruling out potential false-positive results due to differential plasmid uptake by the cells. The third siR-mT circuit effectively suppressed *mTOR* expression (Fig. S7F-S7H) and was therefore selected for further study. Given the critical role of the *mTOR* signaling in regulating tumor cell proliferation and anti-apoptosis, we investigated the effects of the siR-mT circuit on cellular processes. EdU assays and Annexin V/PI staining demonstrated that the siR-mT circuit significantly inhibited proliferation and promoted apoptosis in Renca cells (Fig. S7I–S7L).

Subsequently, we examined the *in vivo* self-assembly and secretion of mTOR siRNA-encapsulating sEVs. After intravenous administration of the siR-mT circuit, mTOR siRNA was detected in the plasma, peaking at approximately 6 h and returning to baseline by 48 h (Fig. S7M). These circulating mTOR siRNAs were confirmed to be encapsulated within sEVs (Fig. S7N). When these plasma-derived sEVs from siR-mT-injected mice were added to Renca cell culture, they effectively downregulated *mTOR* expression (Fig. S7O–S7Q), inhibited proliferation (Fig. S7R–S7S), and induced apoptosis (Fig. S7T–S7U). These findings demonstrated that mTOR

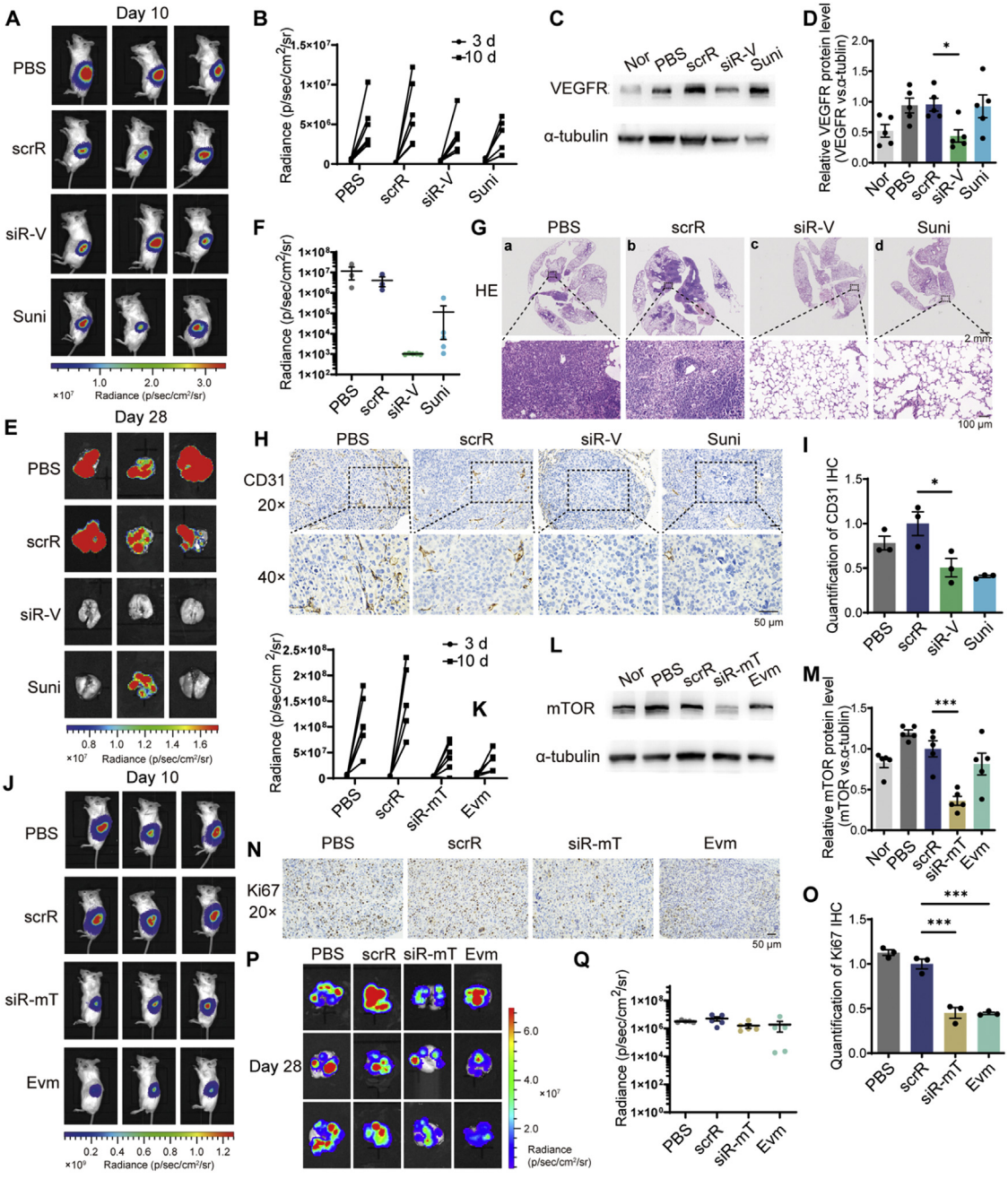


Fig. 3 – Characterization of the IVSA-siRNA targeting *VEGFR2* or *mTOR* in radical nephrectomy ccRCC mice. (A) Luminescent images of mice on Day 10 ($n = 5$); (B) Quantitative BLI results for each mouse ($n = 5$); (C) WB of VEGFR2 protein expression; (D) Quantification of relative VEGFR2 protein level ($n = 5$); (E) Luminescent images of lung metastases on Day 28 ($n = 3$–5); (F) Quantitative BLI results for lung metastases ($n = 3$–5); (G) (a-b) H&E staining at 40× and 100× magnifications demonstrate epithelial-like structures with cellular atypia and focal nests or cord-like arrangements. These features are consistent with a metastatic carcinoma. (c-d) Demonstrate normal lung tissue. Scale bar: 2 mm (upper panel) and 100 μm (lower panel); (H) Lung metastatic tumor sections stained for CD31. Scale bar: 50 μm; (I) Quantification of CD31-positive murine endothelial cells ($n = 3$); (J) Representative luminescent images of mice on Day 10 ($n = 5$); (K) Quantitative BLI results for each mouse ($n = 5$); (L) WB of mTOR protein expression; (M) Quantification of relative mTOR protein level ($n = 5$); (N) Images of orthotopic tumor sections stained with Ki67. Scale bar: 50 μm; (O) Relative quantification of Ki67-positive cells ($n = 3$); (P) Representative luminescent images of lung metastases on Day 28 ($n = 5$); (Q) Quantitative BLI results for lung metastases ($n = 5$). Values are presented as the mean ± SEM. Significance was determined using one-way ANOVA followed by Dunnett's multiple comparison. *P < 0.05; **P < 0.01; ***P < 0.001.

siRNA-encapsulating sEVs were successfully delivered into the mouse bloodstream via siR-mT circuit injection.

Next, we assessed the therapeutic efficacy of IVSA-siRNA targeting *mTOR* in the radical nephrectomy ccRCC model (Fig. S8A). On Day 3, BLI confirmed successful tumor engraftment and a consistent initial tumor burden among all mice (Fig. S8B). Subsequently, the mice were treated every other day from Day 3 with PBS, scrR, siR-mT, or everolimus. All mice underwent radical nephrectomy on Day 10, and lung metastasis was evaluated by BLI on Day 28. In the siR-mT group, we observed e accumulation of mTOR siRNA in the liver, kidney, orthotopic tumor and lung metastatic after 5 injections (Fig. S8C–S8E), which corresponded with significantly reduced mTOR mRNA levels in both orthotopic and lung metastases tumors (Figs. S8F–S8G). Additionally, a marked decrease in the growth rate of orthotopic tumors was observed (Fig. 3J–K and S8H), accompanied by substantial suppression of *mTOR* expression (Fig. 3L-3M and S8I-S8J) and a notable suppression in cell proliferation, as indicated by Ki67 staining (Fig. 3N–3O). Evaluation of lung metastasis by BLI and histology showed a slight, though not statistically significant, reduction in metastatic burden in mice treated with siR-mT circuit or everolimus (Fig. 3P-3Q and S8K). Although the siR-mT circuit effectively inhibited *mTOR* expression in lung metastasis (Fig. S8L-S8M), its ability to suppress lung metastasis appeared relatively lower compared to the siR-V circuit or sunitinib (Fig. 3). Overall, IVSA-siRNA targeting *mTOR* effectively downregulate *mTOR* expression and significantly inhibited the proliferation of orthotopic tumors.

3.5. *Characterization of the IVSA-siRNAs co-targeting VEGFR2 and mTOR*

Based on the aforementioned findings, IVSA-siRNA targeting *VEGFR2* or *mTOR* respectively recapitulated the advantages of sunitinib and everolimus in inhibiting lung metastasis and suppressing tumor proliferation. To achieve simultaneous inhibition of *VEGFR2* and *mTOR*, a genetic circuit was designed comprising two sequential siRNA expression cassettes arranged in a head-to-tail tandem array under a single CMV promoter for concurrent expression of VEGFR2 siRNA and mTOR siRNA (siR-V+mT) (Figs. S4C and Tables S1&S2). We validated the efficacy of the siR-V+mT circuit in EOMA and Renca cells. In EOMA cells, the siR-V+mT circuit exhibited a similar degree of suppression of VEGFR2 mRNA and protein expression as the siR-V circuit (Fig. S9A-S9C). Similarly, in Renca cells, the siR-V+mT circuit demonstrated comparable suppression of *mTOR* expression to that of the siR-mT circuit (Fig. S9D-S9F). Furthermore, the siR-V+mT circuit inhibited EOMA cell proliferation and HUVEC cell angiogenesis (Fig. S9G-S9J). and also suppressed Renca cell proliferation and promoted apoptosis (Fig. S9K–S9N).

To validate the co-assembly of VEGFR2 siRNA and mTOR siRNA into plasma sEVs following intravenous siR-V+mT circuit injection, we investigated the *in vivo* distribution of these sEVs (Fig. 4A). After intravenous administration of the siR-V+mT circuit, both VEGFR2 siRNA and mTOR siRNA were detected in mouse plasma and plasma-derived sEVs (Fig. Fig. 4B–4C and S9O-S9P). The isolated plasma sEVs exhibited characteristics similar to normal sEVs (Fig. S10A-S10B) with sEV markers (CD9, CD63, and TSG101) detected exclusively in the purified sEVs but not in sEV-free plasma (Fig. S10C). Co-culture of these plasma sEVs with EOMA and HUVEC cells significantly reduced *VEGFR2* expression in EOMA cells (Fig. 4D–E and S9Q) and inhibited EOMA cell proliferation and HUVEC angiogenesis (Fig. 4F–4I). Similarly, treatment of Renca cells with these sEVs led to a marked suppression of *mTOR* expression (Fig. 4J-4K and S9R), decreased tumor cell growth (Fig. 4L–4M), and increased apoptosis (Fig. 4N-4O). These results demonstrate that the siR-V+mT circuit successfully generates sEVs containing both VEGFR2 siRNA and mTOR siRNA, which systemically circulate and inhibit endothelial cell function and tumor cell proliferation.

3.6. *Evaluation of the efficacy and toxicity of IVSA-siRNAs co-targeting VEGFR2 and mTOR in an advanced ccRCC model*

To evaluate the therapeutic effects of IVSA-siRNAs co-targeting *VEGFR2* and *mTOR*, the siR-V+mT circuit was intravenously administered to advanced ccRCC models every other day for five doses (Fig. 5A). After five injections, VEGFR2 siRNA and mTOR siRNA were detected in various tissues, including the liver, kidney, orthotopic tumor and lung metastatic (Fig. S11A-S11F). Correspondingly, the mRNA levels of *VEGFR2* and *mTOR* were significantly suppressed in both orthotopic tumors and lung metastatic tumors (Fig. S11G-S11J). BLI on Day 3 confirmed consistent tumor engraftment among all mice (Fig. S12A). Following administration of the siR-V+mT circuit, the median survival increased from 23 d to 62 d when compared to the scrR group, a notable increase in the survival rate of advanced ccRCC mice was observed (Fig. 5B). Furthermore, the siR-V+mT circuit markedly inhibited orthotopic tumor growth. BLI on Day 28 revealed that the orthotopic tumor size in the siR-V+mT group was reduced by 81% compared to the size of the PBS and scrR groups (Fig. 5C–5D). Concomitantly, BLI on Day 28 revealed that the lung fluorescence intensity in the siR-V+mT group shrank by 71% compared to that in the scrR group, indicating a markedly lower burden of lung metastasis (Fig. 5E–5G).

Subsequently, we assessed the toxicity of the siR-V+mT circuit in the advanced ccRCC model. Treatment with the siR-V+mT circuit did not induce significant in body weight changes (Fig. 5H). Echocardiographic and histopathological analyses revealed no signs of cardiotoxicity (Fig. 5I-5L and S12B-S12K). No significant alterations were observed in liver weight or serum levels of AST, ALP and ALT (Fig. 5M-5N and S12L-S12M). Additionally, the TUNEL assay and histological staining demonstrated no apparent apoptosis or immune cells infiltration in the liver (Fig. S12N-S12P). Moreover, serum levels of cholesterol, triglycerides and free fatty acids remained within normal ranges (Fig. 5O–5Q). Finally, histopathological examination of lung sections revealed no signs of foamy cell changes or immune cell infiltration (Fig. 5R and S12Q). Collectively, these results suggest that IVSA-siRNAs co-targeting *VEGFR2* and *mTOR* achieved robust therapeutic efficacy in advanced ccRCC mice without inducing toxic reactions associated with sunitinib and everolimus combination therapy.

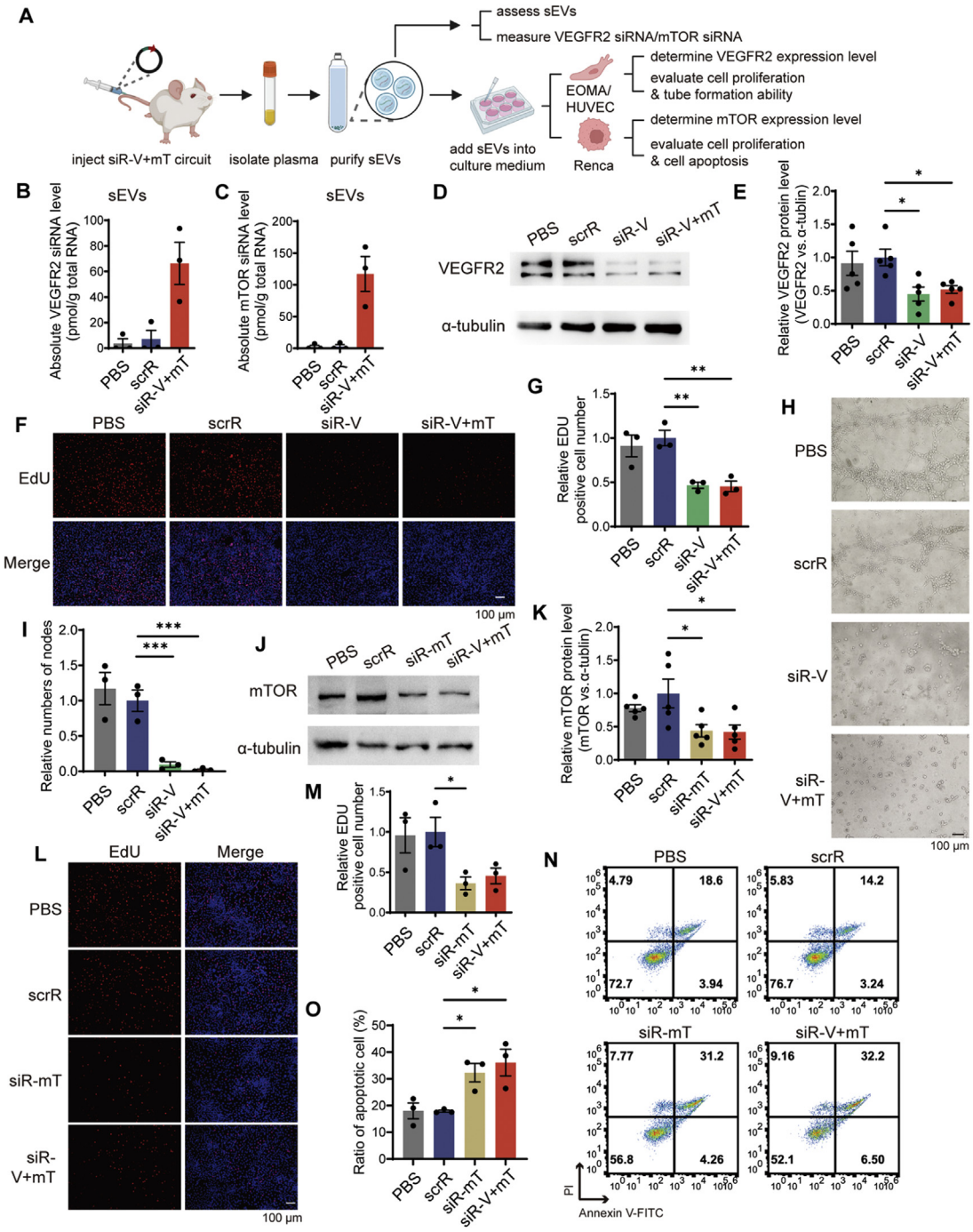


Fig. 4 – Characterization of the IVSA-siRNA co-targeting *VEGFR2* and *mTOR* in an *ex vivo* model. (A) Schematic illustration of the experimental design; (B) Quantitative RT-PCR analysis of VEGFR2 siRNA in sEVs ($n = 3$); (C) Quantitative RT-PCR analysis of mTOR siRNA in sEVs ($n = 3$); (D) WB of VEGFR2 protein expression; (E) Quantification of relative VEGFR2 protein level ($n = 5$); (F) EdU staining of EOMA cells. Scale bar: 100 μm; (G) Quantification of the relative proportion of EdU-positive cells ($n = 3$); (H) Angiogenesis assay. Scale bar: 100 μm; (I) Quantification of the number of nodes ($n = 3$); (J) WB of mTOR protein expression; (K) Quantification of relative mTOR protein level ($n = 5$); (L) EdU staining of Renca cells. Scale bar: 100 μm; (M) Quantification of the relative proportion of EdU-positive cells ($n = 3$); (N) Images of cellular apoptosis analyzed by flow cytometry; (O) Quantification of the rate of apoptotic cells ($n = 3$). Values are presented as the mean ± SEM. Significance was determined using one-way ANOVA followed by Dunnett's multiple comparison. *P < 0.05; **P < 0.01; ***P < 0.001.

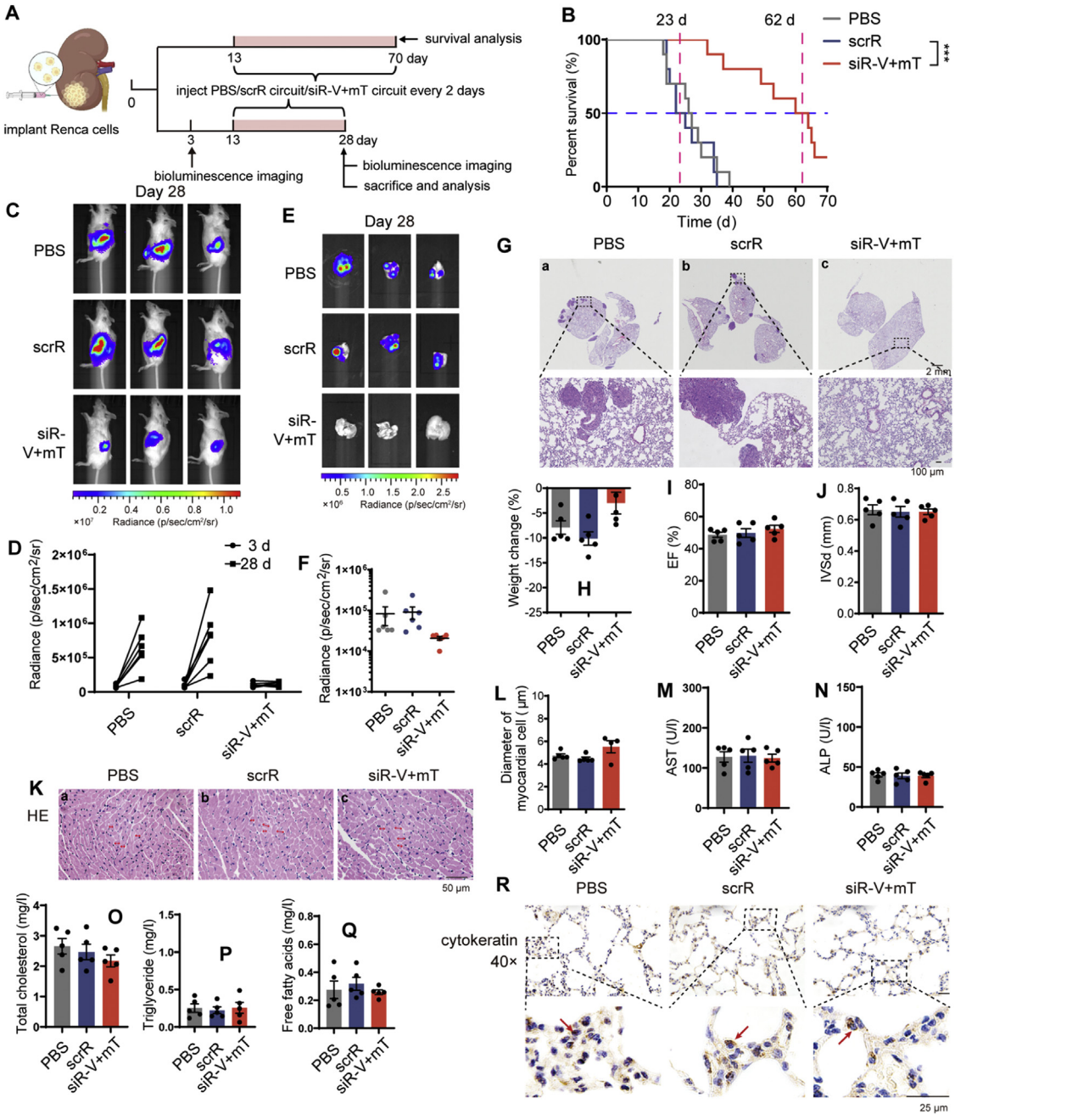


Fig. 5 – Characterization of the IVSA-siRNA co-targeting *VEGFR2* and *mTOR* in advanced ccRCC mice. (A) Schematic illustration of the experimental design; (B) Kaplan-Meier survival curves ($n = 10$), the dashed lines at 23 d and 62 d indicate the median survival duration for the PBS group and siR-V+mT group, respectively; Luminescent images of (C) mice and (E) lung metastases on Day 28 ($n = 6$); Quantitative BLI results for (D) each mouse ($n = 6$) and (F) lung metastases ($n = 6$); (G) (a–b) H&E staining at 40× and 100× magnifications demonstrate epithelial-like structures with cellular atypia and focal nests or cord-like arrangements. These features are consistent with a metastatic carcinoma. (c) Demonstrates normal lung tissue. Scale bar: 2 mm (upper panel) and 100 μm (lower panel); (H) Ratio of body weight change ($n = 5$); (I) Left ventricular EF of treated mice ($n = 5$); (J) Interventricular septal thickness in end-diastole (IVSd) ($n = 5$); (K) (a-c) H&E staining at 100× magnifications demonstrate normal myocardial tissue. The red double arrows indicate the cross-sectional area of cardiomyocytes, highlighting the morphological changes. Scale bar: 50 μm; (L) Average diameter of myocardial cells ($n = 4$–5); Serum (M) AST and (N) ALP enzyme activity ($n = 5$); (O) Total cholesterol, (P) triglyceride and (Q) free fatty acid levels in serum ($n = 5$); (R) Images of lung sections stained with cytokeratin. Arrows indicate hyperplastic enlarged foamy pneumocytes. Scale bar: 25 μm. Values are presented as the mean ± SEM. Significance was determined using one-way ANOVA followed by Dunnett's multiple comparison or Kaplan-Meier test for survival analysis. *$P < 0.05$.

3.7. *Evaluation of the efficacy of IVSA-siRNAs co-targeting VEGFR2 and mTOR in a radical nephrectomy ccRCC model*

We assessed the therapeutic effects of IVSA-siRNAs co-targeting *VEGFR2* and *mTOR* in a radical nephrectomy ccRCC model (Fig. 6A). BALB/c mice were implanted with Luc-Renca cells underneath the renal capsule. After confirming successful tumor engraftment by BLI on Day 3, mice were randomly divided into experimental groups and received intravenous injections of scrR, siR-V, siR-mT or siR-V+mT, or oral administration of PBO or Combo (sunitinib and everolimus) once every 2 d. All mice underwent radical nephrectomy on Day 10. One cohort was monitored for survival until 80 d, and another was euthanized for analysis of tumor growth and target gene knockdown on Day 28.

Compared to scrR-treated mice, the overall survival rate slightly improved in those receiving siR-V or siR-mT, whereas a significant survival advantage was observed in those receiving siR-V+mT, increasing the median survival from 30 d to 80 d (Fig. 6B). Although Combo treatment also significantly improved survival, its efficacy was weaker than that of siR-V+mT, with a median survival that was 22 d shorter. Analysis of body weight changes revealed that treatment with the siR-V+mT circuit did not cause significant weight loss, in contrast to the marked reduction observed in other groups (Fig. S13A). BLI assessment of tumor growth before radical nephrectomy showed extensive tumor burden in mice treated with scrR, siR-V or PBO (Fig. 6C–6D). Conversely, the mice treated with siR-V+mT or Combo exhibited a significant deceleration in tumor growth, reducing tumor sizes by 86% and 69% compared to the control, respectively (Fig. 6C-6D and S13B). Impressively, the mice treated with the siR-V+mT circuit demonstrated minimal tumor growth prior to radical nephrectomy (Fig. 6C–6D). At the molecular level, WB confirmed a significant reduction in VEGFR2 protein and its downstream effector p-PI3K and subsequent p-AKT proteins involved in angiogenesis, along with a reduction in mTOR protein and its downstream proliferative markers p-S6K and p-AKT proteins in the tumors from siR-V+mT-treated mice (Fig. 6E-6H and S13C-S13G). Additionally, CD31 and Ki67 staining revealed a noticeable decreased angiogenesis and cell proliferation in the tumors following siR-V+mT treatment (Fig. 6I–6L).

Regarding the metastatic tumors in the lungs, BLI on Day 28 revealed substantial lung metastasis in radical nephrectomy ccRCC mice treated with scrR or PBO, despite all mice undergoing radical nephrectomy on Day 10. Reduced metastasis was observed in mice treated with siR-V, siR-mT, siR-V+mT and Combo, with the most notable efficacy observed in the siR-V+mT group, the incidence of lung metastasis in this group was reduced by 99% compared to that in the control group, demonstrating a significantly lower metastasis burden than the Combo group. (Fig. 7A–7B). Histological analysis of lung sections revealed that siR-V+mT-treated mice exhibited the lowest level of tumor metastasis (Fig. 7C). WB further confirmed a significant reduction in VEGFR2 protein and its downstream effector p-PI3K and subsequent p-AKT proteins involved in angiogenesis, along with a reduction in mTOR protein and its downstream proliferative markers p-S6K and p-AKT proteins in the lung metastatic from siR-V+mT-treated mice (Fig. 7D-7G and S13H-S13K). Additionally, lung metastases from siR-V+mT-treated mice showed markedly reduced CD31 and Ki67 levels (Fig. 7H–7K), suggesting comprehensive inhibition of metastasis through the concurrent suppression of neovascularization and tumor cell proliferation. Overall, these results indicate that siR-V+mT treatment in the radical nephrectomy ccRCC model successfully suppresses *VEGFR2* and *mTOR* expression, thereby reducing mortality, cancer recurrence rate, and lung metastasis following surgery. Therefore, IVSA-siRNAs co-targeting *VEGFR2* and *mTOR* represent a promising neoadjuvant or adjuvant therapeutic approach for ccRCC.

3.8. *Discussion*

RCC is the most prevalent malignant tumor in the urinary system, characterized by its intrinsic resistance to chemoradiotherapy and a high propensity for distant metastasis [3,51]. The current treatment paradigm for RCC primarily relies on surgical intervention, complemented by molecular targeted therapies to mitigate surgical risks, impede metastatic progression following radical nephrectomy, and manage advanced disease stages [3,25,64]. However, the development of conventional combination therapy has been significantly hampered by the emergence of resistance and associated toxicities linked to molecular targeted therapies [65]. In contrast, gene therapy utilizing siRNA, a novel modality of targeted therapy, has demonstrated promising potential in addressing various diseases [66,67]. Despite this, a major challenge in siRNA-based therapy lies in the lack of a reliable *in vivo* delivery system [68]. In this study, we developed IVSA-siRNAs that emulate the natural packaging process of miRNA cargoes into sEVs as mediated by endogenous cellular machinery. By capitalizing on the inherent capacity of the small RNA processing machinery in the host liver to self-assemble siRNAs into sEVs, as well as leveraging the endogenous circulatory system of sEVs for siRNA transport, we engineered genetic circuits to induce the mouse liver to self-assemble siRNAs into secretory sEVs. These siRNA-encapsulating sEVs were subsequently delivered to tumor tissues and metastatic sites via the bloodstream, resulting in significant reductions in target gene expression and effective suppression of cancer growth and metastasis.

Compared to *in vitro* pre-assembled synthetic siRNAs, IVSA-siRNAs offer superior bioavailability and efficacy, owing to their efficient utilization of the RNAi pathway and sEV circulation system [48]. The IVSA-siRNAs enhance the safety and efficacy of siRNA delivery by generating endogenous, siRNA-loaded sEVs with low immunogenicity, and they enable simultaneous targeting of multiple pathways, which may reduce off-target effects. Thus, IVSA-siRNAs represent a versatile and effective platform for multi-target combination therapy, with broad potential for comprehensive treatment and personalized medicine, its production is also cost-effective, relying on straightforward bacterial culture and plasmid extraction. This study introduced an innovative orthotopic transplantation model combined with radical

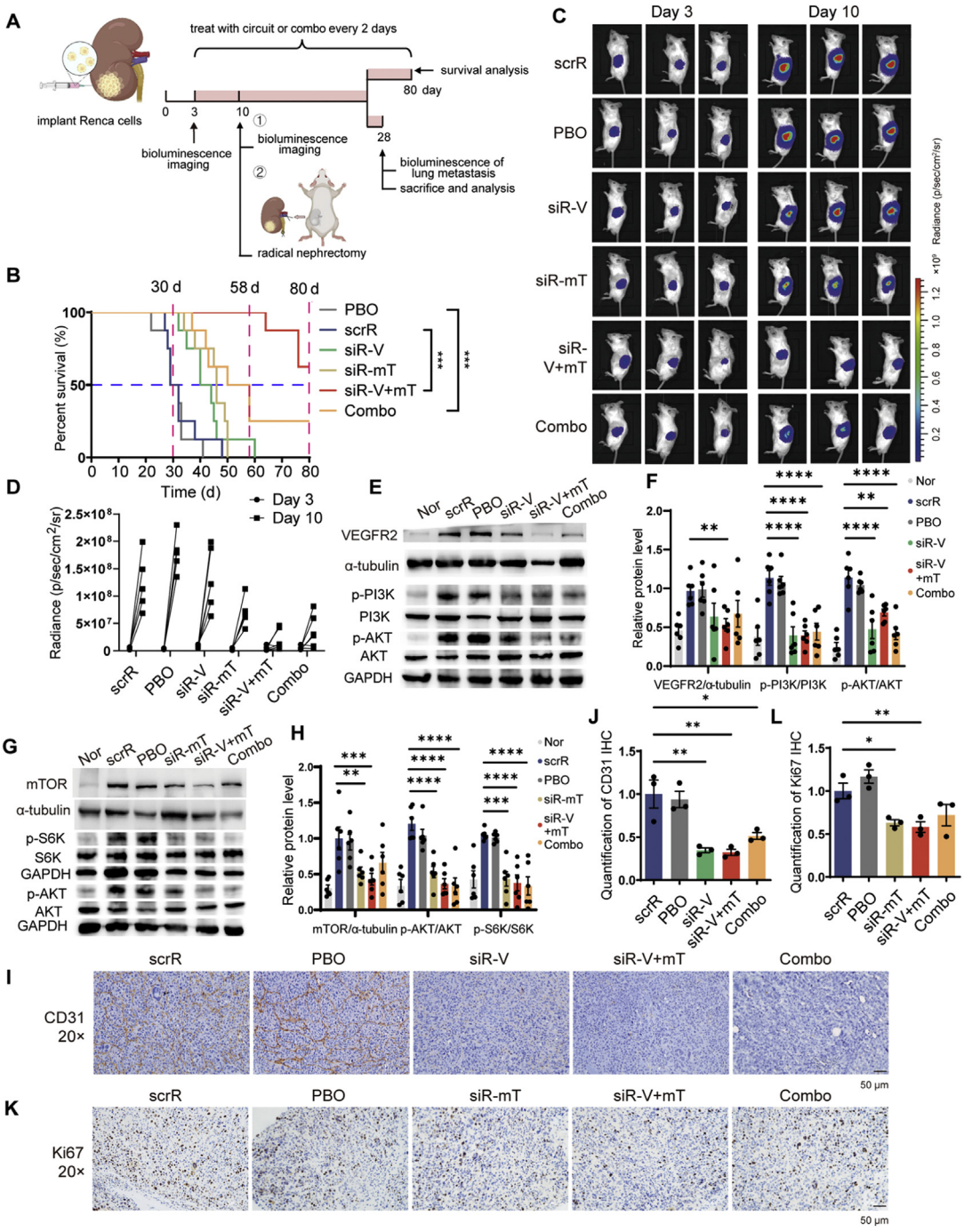


Fig. 6 – Characterization of the IVSA-siRNA co-targeting *VEGFR2* and *mTOR* for inhibiting tumor growth in radical nephrectomy ccRCC mice. (A) Schematic illustration of the experimental design; (B) Kaplan-Meier survival curves ($n = 8$), the dashed lines at 30 d, 58 d and 80 d indicate the median survival duration for the PBO group, Combo group and siR-V+mT group, respectively; (C) Luminescent images of mice on Day 3 and 10; (D) Quantitative BLI results for each mouse ($n = 6$); (E) WB of VEGFR2 pathway protein expression; (F) Quantification of relative VEGFR2 pathway protein level ($n = 6$); (G) WB of mTOR pathway protein expression; (H) Quantification of relative mTOR pathway protein level ($n = 6$); (I) Orthotopic tumor sections stained for CD31. Scale bar: 50 μm; (J) Quantification of CD31-positive endothelial cells ($n = 3$); (K) Images of orthotopic tumor sections stained with Ki67. Scale bar: 50 μm; (L) Relative quantification of Ki67-positive cells ($n = 3$). Values are presented as the mean ± SEM. Significance was determined using one-way ANOVA followed by Dunnett's multiple comparison, or two-way ANOVA followed by Dunnett's test, or Kaplan-Meier test for survival analysis. *$P < 0.05$; **$P < 0.01$; ***$P < 0.001$; ****$P < 0.0001$.

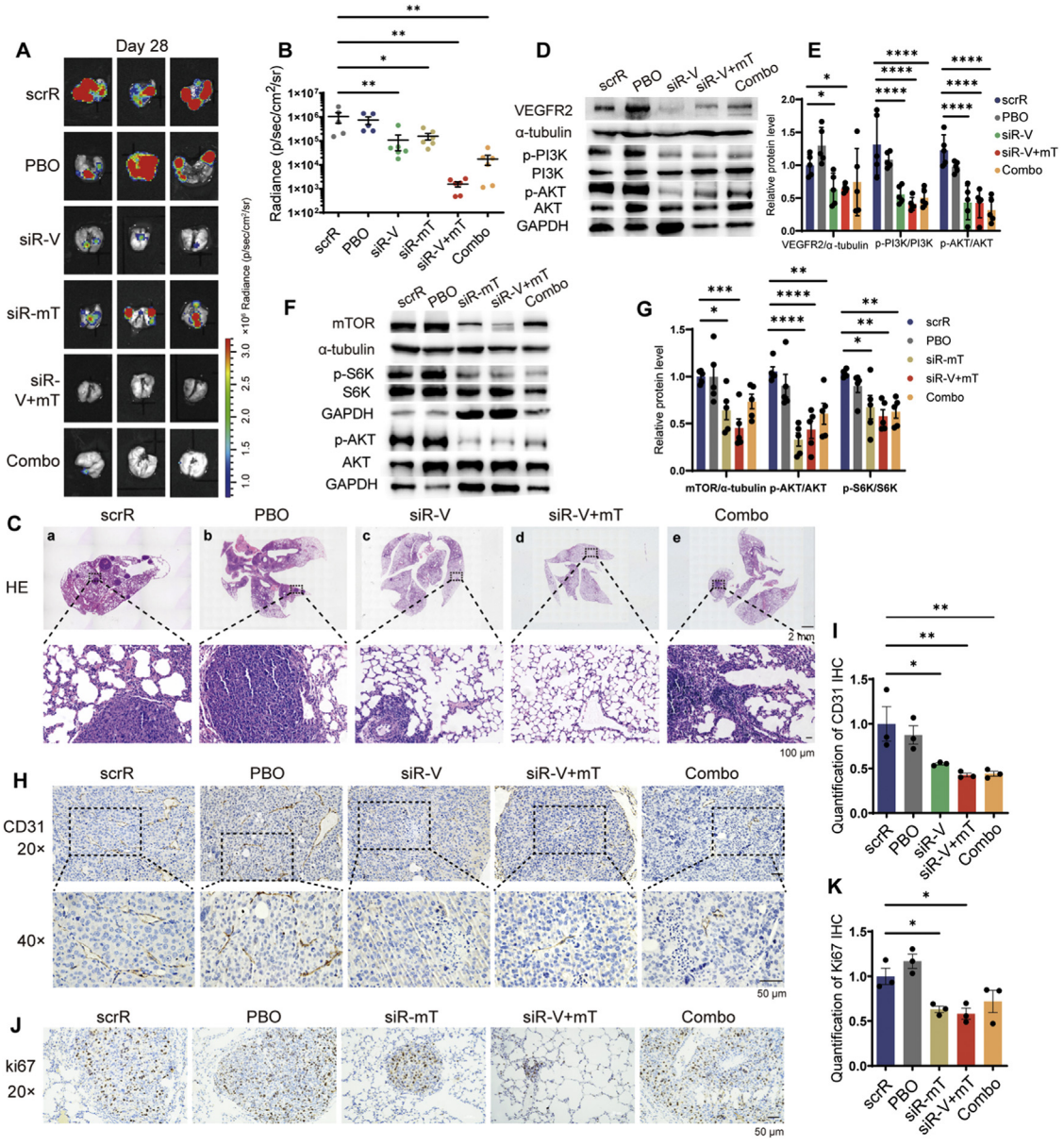


Fig. 7 – Characterization of the IVSA-siRNA co-targeting *VEGFR2* and *mTOR* for inhibiting lung metastases in radical nephrectomy ccRCC mice. (A) Representative luminescent images of lung metastases in different treatment groups on Day 28. (B) Quantitative BLI results for lung metastases ($n = 5–6$). (C) (a-c) and (e) H&E staining at 40× and 100× magnifications demonstrate epithelial-like structures with cellular atypia and focal nests or cord-like arrangements. These features are consistent with a metastatic carcinoma. (d) Demonstrate normal lung tissue Scale bar: 2 mm (upper panel) and 100 μm (lower panel). (D) WB of VEGFR2 pathway protein expression. (E) Quantification of relative VEGFR2 pathway protein level ($n = 5$). (F) WB of mTOR pathway protein expression. (G) Quantification of relative mTOR pathway protein level ($n = 5$). (H) Lung metastatic tumor sections stained for CD31. The figure below is an enlargement of the previously highlighted figure above. Scale bar: 50 μm. (I) Quantification of CD31-positive endothelial cells ($n = 3$). (J) Representative images of lung metastatic tumor sections stained with Ki67. Scale bar: 50 μm. (K) Relative quantification of Ki67-positive cells ($n = 3$). Values are presented as the mean ± SEM. Significance was determined using one-way ANOVA followed by Dunnett's multiple comparison, or two-way ANOVA followed by Dunnett's test. *$P < 0.05$; **$P < 0.01$; ***$P < 0.001$; ****$P < 0.0001$.

nephrectomy to mimic clinical RCC management, enabling a thorough assessment of IVSA-siRNA efficacy and safety.

Several limitations warrant consideration. First, we did not explore targets related to tumor immunotherapy [69]. Our focus on *VEGFR2* and *mTOR* was based on their established roles in ccRCC pathogenesis, providing a solid foundation for evaluating our platform. Future studies should develop IVSA-siRNAs for immunotherapeutic applications. Second, the Renca cell transplantation model has limited genetic and histological heterogeneity. In contrast, patient-derived

xenograft (PDX) models via renal capsule transplantation offer a more representative system for RCC research [70]. Future work should evaluate IVSA-siRNAs tailored to individual tumor gene expression profiles in PDX models. Identifying optimal target gene combinations for personalized therapy will be essential. Advances in single-cell sequencing and artificial intelligence could further refine the efficacy and safety of IVSA-siRNA-based personalized RCC treatment [71,72].

4. Conclusions

In summary, we demonstrated that the siR-V+mT circuit, which integrates VEGFR2 and mTOR siRNA expression cassettes, effectively produces sEVs loaded with VEGFR2 siRNA and mTOR siRNA. Following intravenous administration, the circuit generates and delivers IVSA-siRNAs to orthotopic tumors and lung metastasis, inhibiting tumor growth and neovascularization. Our results show that the siR-V+mT circuit effectively suppresses tumor progression in advanced ccRCC models, while significantly reducing systemic side effects and organ damage. Furthermore, this strategy provides an effective neoadjuvant and adjuvant therapy by reducing cancer recurrence rates and the incidence of lung metastasis after radical nephrectomy.

Conflicts of interest

The authors declare that there is no conflicts of interest.

CRediT authorship contribution statement

Jinyu Fu: Writing – review & editing, Methodology, Investigation, Formal analysis, Data curation. **Xinyan Zhou:** Writing – review & editing, Writing – original draft, Visualization, Validation, Supervision, Software, Resources, Methodology, Investigation, Formal analysis, Data curation. **Junjie Mi:** Methodology, Investigation, Formal analysis, Data curation. **Likun Zhou:** Investigation, Data curation. **Luzhen Ma:** Formal analysis, Data curation. **Jingwei Guo:** Formal analysis, Data curation. **Jieqiong Lei:** Formal analysis, Data curation. **Shuang Qu:** Formal analysis, Data curation. **Zheng Fu:** Conceptualization. **Tianyao Liu:** Resources. **Xi Chen:** Writing – review & editing, Project administration, Funding acquisition, Conceptualization. **Rong Yang:** Writing – review & editing, Resources, Project administration, Methodology, Conceptualization.

Acknowledgments

This work was supported by grants from the National Natural Science Foundation of China (No. 32022015, 31871295 and 82373158), the Training Program of the Major Research Plan of the National Natural Science Foundation of China (No. 92268120), the Starry Night Science Fund of Zhejiang University Shanghai Institute for Advanced Study (No. SN-ZJU-SIAS-008) and CAMS Innovation Fund for Medical Sciences (No. CIFMS-2021-I2M-5–015).

Supplementary materials

Supplementary material associated with this article can be found, in the online version, at doi:10.1016/j.ajps.2026.101126. The figures and tables with “S” before the serial number are included in the Supplementary data.

REFERENCES

[1] Siegel RL, Miller KD, Jemal A. Cancer statistics, 2019. CA Cancer J Clin 2019;69(1):7–34.
[2] Hahn AW, Klaassen Z, Agarwal N, Haaland B, Esther J, Ye XY, et al. First-line treatment of metastatic renal cell carcinoma: a systematic review and network meta-analysis. Eur Urol Oncol 2019;2(6):708–15.
[3] Hsieh JJ, Purdue MP, Signoretti S, Swanton C, Albiges L, Schmidinger M, et al. Renal cell carcinoma. Nat Rev Dis Primers 2017;3:17009.
[4] Veeratterapillay R, Simren R, El-Sherif A, Johnson MI, Soomro N, Heer R. Accuracy of the revised 2010 TNM classification in predicting the prognosis of patients treated for renal cell cancer in the north east of England. J Clin Pathol 2012;65(4):367–71.
[5] Ljungberg B, Albiges L, Abu-Ghanem Y, Bedke J, Capitanio U, Dabestani S, et al. European association of urology guidelines on renal cell carcinoma: the 2022 update. Eur Urol 2022;82(4):399–410.
[6] Jonasch E, Gao J, Rathmell WK. Renal cell carcinoma. BMJ 2014;349:g4797.
[7] Luciani LG, Porpiglia F, Cai T, D'Elia C, Vattovani V, Giusti G, et al. Operative safety and oncologic outcome of laparoscopic radical nephrectomy for renal cell carcinoma >7 cm: a multicenter study of 222 patients. Urology 2013;81(6):1239–44.
[8] Verhoest G, Couapel JP, Oger E, Rioux-Leclercq N, Pignot G, Patard JJ, et al. Safety and feasibility of laparoscopic nephrectomy for big tumors (≥ 10 cm): a retrospective multicentric study. Clin Genitourin Cancer 2016;14(4):e335–40.
[9] Stewart GD, Welsh SJ, Ursprung S, Gallagher FA, Jones JO, Shields J, et al. A phase II study of neoadjuvant axitinib for reducing the extent of venous tumour thrombus in clear cell renal cell cancer with venous invasion (NAXIVA). Br J Cancer 2022;127(6):1051–60.
[10] Bex A, van Thienen JV, Schrier M, Graafland N, Kuusk T, Hendricksen K, et al. A phase II, single-arm trial of neoadjuvant axitinib plus avelumab in patients with localized renal cell carcinoma who are at high risk of relapse after nephrectomy (NEOAVAX). Fut Oncol 2019;15(19):2203–9.
[11] Powles T, Tomczak P, Park SH, Venugopal B, Ferguson T, Symeonides SN, et al. Pembrolizumab *versus* placebo as post-nephrectomy adjuvant therapy for clear cell renal cell carcinoma (KEYNOTE-564): 30-month follow-up analysis of a multicentre, randomised, double-blind, placebo-controlled, phase 3 trial. Lancet Oncol 2022;23(9):1133–44.
[12] Allison SJ. Kidney cancer: targeting metabolism in RCC. Nat Rev Nephrol 2017;13(6):320.
[13] Sciarra A, Cattarino S, Salciccia S, Alfarone A, Gentilucci A, Parente U, et al. The emerging role of targeted therapy in renal cell carcinoma (RCC): is it time for a neoadjuvant or an adjuvant approach? Crit Rev Oncol Hematol 2012;81(2):151–62.

[14] Hakozaki T, Okuma Y, Omori M, Hosomi Y. Impact of prior antibiotic use on the efficacy of nivolumab for non-small cell lung cancer. Oncol Lett 2019;17(3):2946–52.
[15] Kocarnik JM, Compton K, Dean FE, Fu W, Gaw BL, Harvey JD, et al. Cancer incidence, mortality, years of life lost, years lived with disability, and disability-adjusted life years for 29 cancer groups from 2010 to 2019: a systematic analysis for the global burden of disease study 2019. JAMA Oncol 2022;8(3):420–44.
[16] Liu GH, Chen T, Zhang X, Ma XL, Shi HS. Small molecule inhibitors targeting the cancers. MedComm 2020;3(4):e181 2022.
[17] Gharwan H, Groninger H. Kinase inhibitors and monoclonal antibodies in oncology: clinical implications. Nat Rev Clin Oncol 2016;13(4):209–27.
[18] Cook KM, Figg WD. Angiogenesis inhibitors: current strategies and future prospects. CA Cancer J Clin 2010;60(4):222–43.
[19] Granovetter M. Multitarget pharmacological inhibition for renal cell carcinoma. Lancet Oncol 2016;17(4):e140.
[20] Jin H, Wang L, Bernards R. Rational combinations of targeted cancer therapies: background, advances and challenges. Nat Rev Drug Discov 2023;22(3):213–34.
[21] Parhi P, Mohanty C, Sahoo SK. Nanotechnology-based combinational drug delivery: an emerging approach for cancer therapy. Drug Discov Today 2012;17(17–18):1044–52.
[22] Greco F, Vicent MJ. Combination therapy: opportunities and challenges for polymer-drug conjugates as anticancer nanomedicines. Adv Drug Deliv Rev 2009;61(13):1203–13.
[23] Schwartz CL, Gorlick R, Teot L, Krailo M, Chen Z, Goorin A, et al. Multiple drug resistance in osteogenic sarcoma: INT0133 from the children's oncology group. J Clin Oncol 2007;25(15):2057–62.
[24] Van Meir EG, Hadjipanayis CG, Norden AD, Shu HK, Wen PY, Olson JJ. Exciting new advances in neuro-oncology: the avenue to a cure for malignant glioma. CA Cancer J Clin 2010;60(3):166–93.
[25] Molina AM, Lin X, Korytowsky B, Matczak E, Lechuga MJ, Wiltshire R, et al. Sunitinib objective response in metastatic renal cell carcinoma: analysis of 1059 patients treated on clinical trials. Eur J Cancer 2014;50(2):351–8.
[26] Motzer RJ, Hutson TE, McCann L, Deen K, Choueiri TK. Overall survival in renal-cell carcinoma with pazopanib *versus* sunitinib. N Engl J Med 2014;370(18):1769–70.
[27] Motzer RJ, Barrios CH, Kim TM, Falcon S, Cosgriff T, Harker WG, et al. Phase II randomized trial comparing sequential first-line everolimus and second-line sunitinib *versus* first-line sunitinib and second-line everolimus in patients with metastatic renal cell carcinoma. J Clin Oncol 2014;32(25):2765–72.
[28] Molina AM, Feldman DR, Voss MH, Ginsberg MS, Baum MS, Brocks DR, et al. Phase 1 trial of everolimus plus sunitinib in patients with metastatic renal cell carcinoma. Cancer 2012;118(7):1868–76.
[29] Motzer RJ, Hutson TE, Glen H, Michaelson MD, Molina A, Eisen T, et al. Lenvatinib, everolimus, and the combination in patients with metastatic renal cell carcinoma: a randomised, phase 2, open-label, multicentre trial. Lancet Oncol 2015;16(15):1473–82.
[30] Matsubara N, Naito Y, Nakano K, Fujiwara Y, Ikezawa H, Yusa W, et al. Lenvatinib in combination with everolimus in patients with advanced or metastatic renal cell carcinoma: a phase 1 study. Int J Urol 2018;25(11):922–8.
[31] Bendtsen MAF, Grimm D, Bauer J, Wehland M, Wise P, Magnusson NE, et al. Hypertension caused by lenvatinib and everolimus in the treatment of metastatic renal cell carcinoma. Int J Mol Sci 2017;18(8):1736.
[32] Patel PH, Senico PL, Curiel RE, Motzer RJ. Phase I study combining treatment with temsirolimus and sunitinib malate in patients with advanced renal cell carcinoma. Clin Genitourin Cancer 2009;7(1):24–7.
[33] Turgutalp B, Kizil C. Multi-target drugs for Alzheimer's disease. Trends Pharmacol Sci 2024;45(7):628–38.
[34] Deeks SG, Archin N, Cannon P, Collins S, Jones RB, de Jong M, et al. Research priorities for an HIV cure: international AIDS Society global scientific strategy 2021. Nat Med 2021;27(12):2085–98.
[35] Al-Lazikani B, Banerji U, Workman P. Combinatorial drug therapy for cancer in the post-genomic era. Nat Biotechnol 2012;30(7):679–92.
[36] Two-drug cocktail active against RCC. Cancer Discov 2019;9(1):6.
[37] Sokolov AV, Dostdar SA, Attwood MM, Krasilnikova AA, Ilina AA, Nabieva AS, et al. Brain cancer drug discovery: clinical trials, drug classes, targets, and combinatorial therapies. Pharmacol Rev 2021;73(4):1–32.
[38] Kim YD, Park TE, Singh B, Maharjan S, Choi YJ, Choung PH, et al. Nanoparticle-mediated delivery of siRNA for effective lung cancer therapy. Nanomedicine (Lond) 2015;10(7):1165–88.
[39] Lee RC, Feinbaum RL. Ambros V. The C. elegans heterochronic gene lin-4 encodes small RNAs with antisense complementarity to lin-14. Cell 1993;75(5):843–54.
[40] Zhou X, Yu M, Ma L, Fu J, Guo J, Lei J, et al. *In vivo* self-assembled siRNA as a modality for combination therapy of ulcerative colitis. Nat Commun 2022;13(1):5700.
[41] Tang W, Chen Y, Jang HS, Hang Y, Jogdeo CM, Li J, et al. Preferential siRNA delivery to injured kidneys for combination treatment of acute kidney injury. J Control Release 2022;341:300–13.
[42] Kanvinde S, Kulkarni T, Deodhar S, Bhattacharya D, Dasgupta A. Non-viral vectors for delivery of nucleic acid therapies for cancer. BioTech (Basel) 2022;11(1):6.
[43] Raguram A, Banskota S, Liu DR. Therapeutic *in vivo* delivery of gene editing agents. Cell 2022;185(15):2806–27.
[44] Bouard D, Alazard-Dany D, Cosset FL. Viral vectors: from virology to transgene expression. Br J Pharmacol 2009;157(2):153–65.
[45] Cullis PR, Hope MJ. Lipid nanoparticle systems for enabling gene therapies. Mol Ther 2017;25(7):1467–75.
[46] van der Meel R, Wender PA, Merkel OM, Lostalé-Seijo I, Montenegro J, Miserez A, et al. Next-generation materials for nucleic acid delivery. Nat Rev Mater 2025;10(7):490–9.
[47] Ali Zaidi SS, Fatima F, Ali Zaidi SA, Zhou D, Deng W, Liu S. Engineering siRNA therapeutics: challenges and strategies. J Nanobiotechnology 2023;21(1):381.
[48] Fu Z, Zhang X, Zhou X, Ur-Rehman U, Yu M, Liang H, et al. *In vivo* self-assembled small RNAs as a new generation of RNAi therapeutics. Cell Res 2021;31(6):631–48.
[49] Jeppesen DK, Fenix AM, Franklin JL, Higginbotham JN, Zhang Q, Zimmerman LJ, et al. Reassessment of exosome composition. Cell 2019;177(2):428–45.
[50] Théry C, Witwer KW, Aikawa E, Alcaraz MJ, Anderson JD, Andriantsitohaina R, et al. Minimal information for studies of extracellular vesicles 2018 (MISEV2018): a position statement of the International Society for Extracellular Vesicles and update of the MISEV2014 guidelines. J Extracell Vesicles 2018;7(1):1535750.
[51] Price M, Wu CC, Genshaft S, Sadow PM, Xie L, Shepard JO, et al. Imaging and management of intrathoracic renal cell carcinoma metastases. AJR Am J Roentgenol 2018;210(6):1181–91.
[52] Chu TF, Rupnick MA, Kerkela R, Dallabrida SM, Zurakowski D, Nguyen L, et al. Cardiotoxicity associated with tyrosine kinase inhibitor sunitinib. Lancet 2007;370(9604):2011–19.
[53] Zhao Q, Zhang T, Xiao XR, Huang JF, Wang Y, Gonzalez FJ, et al. Impaired clearance of sunitinib leads to metabolic disorders and hepatotoxicity. Br J Pharmacol 2019;176(13):2162–78.

[54] Kerkela R, Woulfe KC, Durand JB, Vagnozzi R, Kramer D, Chu TF, et al. Sunitinib-induced cardiotoxicity is mediated by off-target inhibition of AMP-activated protein kinase. Clin Transl Sci 2009;2(1):15–25.
[55] Kokuho N, Terasaki Y, Kunugi S, Saito Y, Urushiyama H, Terasaki M, et al. Analyses of alveolar epithelial injury via lipid-related stress in mammalian target of rapamycin inhibitor-induced lung disease. Lab Invest 2019;99(6):853–65.
[56] Auguste P, Lemiere S, Larrieu-Lahargue F, Bikfalvi A. Molecular mechanisms of tumor vascularization. Crit Rev Oncol Hematol 2005;54(1):53–61.
[57] Simons M, Gordon E, Claesson-Welsh L. Mechanisms and regulation of endothelial VEGF receptor signalling. Nat Rev Mol Cell Biol 2016;17(10):611–25.
[58] Zhang G, Budker V, Wolff JA. High levels of foreign gene expression in hepatocytes after tail vein injections of naked plasmid DNA. Hum Gene Ther 1999;10(10):1735–7.
[59] Lan J, Sun L, Xu F, Liu L, Hu F, Song D, et al. M2 macrophage-derived exosomes promote cell migration and invasion in colon cancer. Cancer Res 2019;79(1):146–58.
[60] Ying W, Riopel M, Bandyopadhyay G, Dong Y, Birmingham A, Seo JB, et al. Adipose tissue macrophage-derived exosomal miRNAs can modulate *in vivo* and *in vitro* insulin sensitivity. Cell 2017;171(2):372–84.
[61] Bala S, Petrasek J, Mundkur S, Catalano D, Levin I, Ward J, et al. Circulating microRNAs in exosomes indicate hepatocyte injury and inflammation in alcoholic, drug-induced, and inflammatory liver diseases. Hepatology 2012;56(5):1946–57.
[62] Alexander M, Hu R, Runtsch MC, Kagele DA, Mosbruger TL, Tolmachova T, et al. Exosome-delivered microRNAs modulate the inflammatory response to endotoxin. Nat Commun 2015;6:7321.
[63] Jeong JH, Ojha U, Lee YM. Pathological angiogenesis and inflammation in tissues. Arch Pharm Res 2021;44(1):1–15.
[64] Motzer RJ, Escudier B, Oudard S, Hutson TE, Porta C, Bracarda S, et al. Efficacy of everolimus in advanced renal cell carcinoma: a double-blind, randomised, placebo-controlled phase III trial. Lancet 2008;372(9637):449–56.
[65] Jin J, Xie Y, Zhang JS, Wang JQ, Dai SJ, He WF, et al. Sunitinib resistance in renal cell carcinoma: from molecular mechanisms to predictive biomarkers. Drug Resist Updat 2023;67:100929.
[66] Kang H, Ga YJ, Kim SH, Cho YH, Kim JW, Kim C, et al. Small interfering RNA (siRNA)-based therapeutic applications against viruses: principles, potential, and challenges. J Biomed Sci 2023;30(1):88.
[67] Hu B, Zhong L, Weng Y, Peng L, Huang Y, Zhao Y, et al. Therapeutic siRNA: state of the art. Signal Transduct Target Ther 2020;5(1):101.
[68] Kanasty R, Dorkin JR, Vegas A, Anderson D. Delivery materials for siRNA therapeutics. Nat Mater 2013;12(11):967–77.
[69] Navani V, Heng DYC. Immunotherapy in renal cell carcinoma. Lancet Oncol 2023;24(11):1164–6.
[70] Patel A, Cohen S, Moret R, Maresh G, Gobe GC, Li L. Patient-derived xenograft models to optimize kidney cancer therapies. Transl Androl Urol 2019;8(Suppl 2):S156–65.
[71] Wiedmeier JE, Noel P, Lin W, Von Hoff DD, Han H. Single-cell sequencing in precision medicine. Cancer Treat Res 2019;178:237–52.
[72] Park JH, Feroze AH, Emerson SN, Mihalas AB, Keene CD, Cimino PJ, et al. A single-cell based precision medicine approach using glioblastoma patient-specific models. NPJ Precis Oncol 2022;6(1):55.